Cell Stem Cell

Article

Comparative single-cell lineage tracing identifies distinct adipocyte precursor dynamics in skin and inguinal fat

Graphical abstract

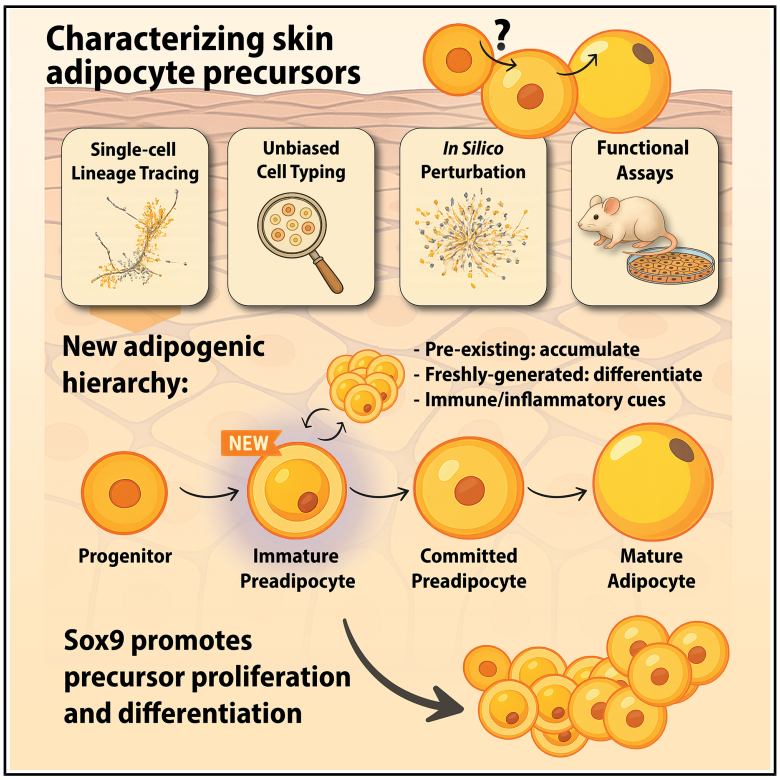

Highlights

- Skin adipocyte precursors differentiate via multiple parallel trajectories
- Progenitors and preadipocytes exhibit distinct lineage dynamics
- Sox9 critically regulates skin adipocyte progenitor differentiation
- Skin adipogenesis is uniquely regulated compared with other adipose depots

Authors

Guillermo C. Rivera-Gonzalez, Emily G. Butka, Carolynn E. Gonzalez, ..., Brett A. Shook, Matthew S. Rodeheffer, Samantha A. Morris

Correspondence

guillermo@capybio.com (G.C.R.-G.), samorris2@bwh.harvard.edu (S.A.M.)

In brief

Morris and colleagues use single-cell lineage tracing to track adipocyte formation in mouse skin. They demonstrate that distinct precursor populations—progenitors and immature preadipocytes—exhibit different potentials for generating mature adipocytes, uncover depot-specific extrinsic regulation, and identify Sox9 as a key intrinsic regulator of skin adipogenesis.

Rivera-Gonzalez et al., 2025, Cell Stem Cell *32*, 1267–1284
August 7, 2025
https://doi.org/10.1016/j.stem.2025.07.004

CellPress

Cell Stem Cell

CellPress
OPEN ACCESS

Article

Comparative single-cell lineage tracing identifies distinct adipocyte precursor dynamics in skin and inguinal fat

Guillermo C. Rivera-Gonzalez,[1,2,3,10,11,*] Emily G. Butka,[1,2,3,10] Carolynn E. Gonzalez,[1,2,3] Rachel L. Mintz,[4] Sarah S. Kleb,[5] Violet Josephson,[5] Wenjun Kong,[1,2,3] Kunal Jindal,[1,2,3,11] Kenji Kamimoto,[1,2,3] Brett A. Shook,[5,6] Matthew S. Rodeheffer,[7] and Samantha A. Morris[8,9,12,*]

[1]Department of Developmental Biology, Washington University School of Medicine, 660 S. Euclid Avenue, St. Louis, MO 63110, USA
[2]Department of Genetics, Washington University School of Medicine, 660 S. Euclid Avenue, St. Louis, MO 63110, USA
[3]Center of Regenerative Medicine, Washington University School of Medicine, 660 S. Euclid Avenue, St. Louis, MO 63110, USA
[4]Department of Biomedical Engineering, Washington University in St. Louis, 6201 Forsyth Blvd, St. Louis, MO 63105, USA
[5]Department of Biochemistry and Molecular Medicine, School of Medicine and Health Sciences, The George Washington University, Washington, DC 20037, USA
[6]Department of Dermatology, School of Medicine and Health Sciences, The George Washington University, Washington, DC 20037, USA
[7]Department of Comparative Medicine, Yale University, New Haven, CT, USA
[8]Division of Gastroenterology, Hepatology and Endoscopy, Division of Genetics, Brigham and Women's Hospital, Boston, MA 02115, USA
[9]Department of Systems Biology, Harvard Medical School, Boston, MA 02115, USA
[10]These authors contributed equally
[11]Present address: CapyBio Inc. 4340 Duncan Avenue, St Louis, MO 63110, USA
[12]Lead contact
*Correspondence: guillermo@capybio.com (G.C.R.-G.), samorris2@bwh.harvard.edu (S.A.M.)
https://doi.org/10.1016/j.stem.2025.07.004

SUMMARY

White adipose tissue supports essential physiological functions through adipocyte precursor cells (APCs), comprising progenitors and preadipocytes, which generate mature adipocytes during depot expansion. Using single-cell RNA sequencing-based lineage tracing, we characterize APCs in skin adipose tissue—a depot uniquely capable of rapid adipogenesis compared with other sites, such as inguinal adipose. We identify a previously uncharacterized population of immature preadipocytes and reveal distinct differentiation potentials among APCs. Contrary to traditional stepwise differentiation models, progenitors predominantly generate committed preadipocytes, whereas preexisting preadipocytes accumulate in immature states with divergent potential. Leveraging this refined APC hierarchy, we uncover Sox9 as a crucial regulator of progenitor proliferation and adipogenic differentiation. Cross-depot transplantation further demonstrates how intrinsic and extrinsic factors differentially regulate skin progenitor behavior, highlighting distinct adipogenic dynamics between skin and inguinal depots. Together, these insights redefine the cellular hierarchy and molecular mechanisms underpinning rapid adipogenesis in skin adipose tissue.

INTRODUCTION

White adipose tissue is essential not only for energy storage and metabolic homeostasis but also actively participates in diverse physiological processes, including immune modulation, tissue repair, fibrosis, and hair follicle regulation.[1–4] Mature adipocytes, specialized cells within adipose tissue, store excess energy as lipids. Adipose tissue expansion occurs via hypertrophy—an increase in adipocyte size—or hyperplasia, the generation of new adipocytes through adipogenesis, which is vital for maintaining tissue homeostasis.[5,6] Since mature adipocytes are typically post-mitotic,[7,8] new adipocytes arise from the proliferation and differentiation of adipocyte precursor cells (APCs), consisting of progenitors and preadipocytes. Historically, APC populations across murine adipose depots were identified through surface markers,[9–12] but recent single-cell RNA sequencing (scRNA-seq) has provided an unbiased approach for classifying these cells.[13–18] For example, committed preadipocytes express *Icam1*, while progenitors express *Dpp4*.[14]

Transplant studies suggest a hierarchical model wherein progenitors give rise to preadipocyte-like cells, assuming synchronous replacement as differentiation progresses. However, adipose depots differ significantly based on anatomical location and biological function.[19] While subcutaneous and visceral depots require up to 8 weeks to produce new adipocytes under a high-fat diet,[20,21] and mammary gland adipose expansion post-lactation primarily occurs via hypertrophy.[22] The dermal depot uniquely generates mature adipocytes within just 11–14 days under

homeostatic conditions.[23,24] This rapid generation of new mature adipocytes in the dermis without an energy surplus activation has not been documented in other adipose depots. Although hair follicles trigger adipogenesis in the skin,[4,23] the existence of depot-specific differences in adipocyte precursors suggests distinct mechanisms of adipogenesis operate uniquely in the skin compared with other adipose depots.[25] Clarifying depot-specific APC characteristics could enable therapeutic strategies to enhance adipogenesis for improved metabolic health.

Deciphering adipogenic differentiation demands high-resolution lineage tracing. Existing APC tracing methods either lack specificity or are limited to small subsets, complicating interpretation. Genetic barcoding technologies thus offer superior resolution for characterizing APC lineages. Here, we employ scRNA-seq of skin adipose tissue combined with fluorescence-activated cell sorting (FACS)-based enrichment of progenitors and preadipocytes. We uncover a previously unrecognized immature preadipocyte population, representing a stable and distinct branch within the skin APC hierarchy. Leveraging our unbiased genetic barcoding strategy, "CellTagging,"[26–29] we track progenitor and preadipocyte differentiation dynamics during homeostatic adipogenesis, revealing progenitors as primary contributors to immature preadipocytes, exhibiting enhanced adipogenic commitment potential.

Unexpectedly, pre-existing preadipocytes harbor distinct transcriptional profiles and divergent differentiation potential, challenging the conventional linear differentiation model. Using this refined hierarchy, we dissect intrinsic and extrinsic factors regulating adipogenesis. We identify Sox9 as a critical cell-intrinsic regulator of APC proliferation and differentiation. Additionally, cross-depot transplantation of skin progenitors into inguinal adipose tissue highlights crucial extrinsic niche factors driving depot-specific adipogenic outcomes. Collectively, these findings reveal previously unknown preadipocyte states, detailed progenitor-preadipocyte dynamics, and intrinsic and niche-dependent mechanisms underlying progenitor differentiation.

RESULTS

Identification of an uncharacterized immature preadipocyte population in the skin

To characterize adipogenesis in the skin, we used scRNA-seq to assess cell type heterogeneity. Given that skin adipogenesis is closely synchronized with the hair follicle cycle,[4,23,24] we performed scRNA-seq on Lin−, CD29+/CD34+ double-positive cells isolated via FACS[12,24,30] from mouse skin at postnatal day 21 (P21). This stage corresponds to the telogen (quiescent) phase of the hair cycle, during which adipogenesis is minimal,[23,24] thereby enriching for progenitor cell types prior to differentiation (Figure 1A). After rigorous quality control and filtering (STAR Methods), we obtained 14,478 high-quality APC transcriptomes (Figure 1B).

To annotate cell identity in an unbiased manner, we applied Capybara, a computational classifier that uses global transcriptomic information to assign identities relative to existing single-cell reference datasets.[31] For this purpose, we integrated published single-cell datasets from various skin and adipose tissues, encompassing diverse adipogenic and fibroblast cell types, creating a consolidated reference atlas (Figures S1A–S1G).[14,18,32–34] Our analysis revealed that 93.7% of P21 skin APCs aligned closely with Merrick et al.'s mouse inguinal adipose dataset[14] or represented transitional states between these defined identities. Importantly, cell identity classification using label transfer produced highly consistent results, with 84.7% of cells receiving the same classification, whether using the consolidated reference or Merrick reference alone (Figures 1C, S1H, and S1I).

We further validated the similarity between our dataset and the Merrick reference by integrating our APC data with each of the five reference datasets individually. Nearest neighbor (NN) analysis in principal component space indicated the Merrick dataset most closely matched the cellular composition observed in our skin APC data. Specifically, mean proportions of P21 skin APCs among 20 NNs to each reference dataset were highest with the Merrick dataset (0.600), indicating the strongest transcriptional similarity (Figure 1D). These results robustly supported the Merrick dataset as the most appropriate reference for subsequent cell classification analyses.

Using this reference, Capybara allowed us to classify our skin adipose populations into two primary groups. The first group consisted of putative progenitor cells (clusters 0, 1, 2, 4, 5, 6, 9, and 10; Figure 1B) that closely corresponded to interstitial progenitor cells in the Merrick reference (Figure 1E). The second, more heterogeneous group comprised putative preadipocytes (clusters 3, 7, 8, and 11), aligning partially with previously described committed preadipocytes. Within this heterogeneous preadipocyte group, we noted alignment with several previously undefined clusters from the Merrick dataset. Notably, our preadipocyte cluster 7 aligned closely with Merrick's inguinal undefined group 3 and committed preadipocytes, whereas cluster 3, exhibiting the highest *F3* expression in our dataset, aligned instead with Merrick's inguinal undefined group 5. This distinction highlighted a previously uncharacterized *F3*-high preadipocyte population distinct from Merrick's original group 3 classification (Figure S1J).

With this classification, we next quantitatively compared cell type composition between skin and inguinal adipose depots. The analysis revealed significant enrichment of interstitial progenitors (85% in skin vs. 22% in inguinal) and particularly undefined group 5 cells (7.4% in skin vs. 2.2% in inguinal; Figure 1E, right). The enriched abundance of undefined group 5 cells is particularly notable given their previously undefined adipogenic potential, having been identified solely based on limited marker expression (*Egfl6* and *Emb*) without detailed functional characterization by Merrick et al.[14]

Moreover, Capybara identified cells exhibiting multiple simultaneous identities ("multi-ID" cells), previously shown to represent transitional differentiation states.[31] We identified 203 multi-ID cells clustering primarily with preadipocytes, most of which (76%) co-expressed identities associated with interstitial progenitors, undefined groups 3 (*F3+/Cd142*), 4, and 5. These multi-ID cells maintained a strong fractional progenitor identity, suggesting transitional states within the adipogenic lineage and reinforcing the adipogenic relevance of undefined group 5 cells (Figures S2A–S2C).

Guided by these findings, we established a refined skin-specific APC classification paradigm (Figures 2A–2C; Table S1). Cells in clusters 0, 1, 2, 4, 5, 6, and 10 represented progenitors, the most immature cells in our atlas. Cells classified by Capybara

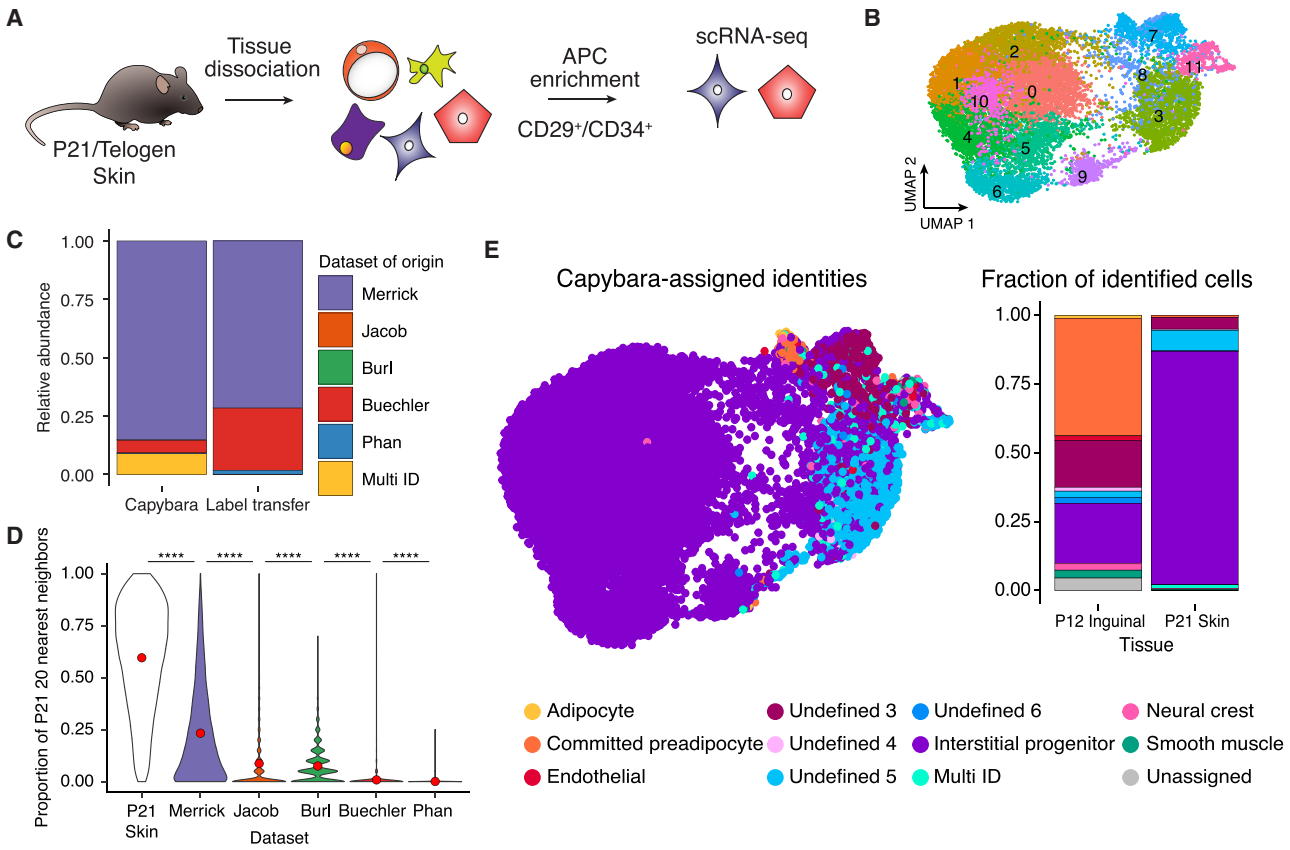

Figure 1. Identification of a putative immature preadipocyte population in skin

(A) Schematic of APC isolation strategy for scRNA-seq profiling.

(B) Uniform manifold approximation and projection (UMAP) of skin-derived APCs (14,478 cells from 2 male and 2 female mice).

(C) Origin of identified cell types by Capybara and label transfer methods using a consolidated reference.

(D) Mean proportion of each dataset among the 20 nearest neighbors (NNs) to P21 skin APCs in co-embedded analyses (***$p < 0.0001$, unpaired t test with Welch's correction).

(E) Capybara classification using the Merrick et al. reference[14] (left) and relative cell type proportions comparing inguinal (reference) and skin datasets (right).

See also Figure S1 and Table S1.

as progenitors but displaying increased *Cd9* expression, characteristic of preadipocytes,[14] were designated transitioning progenitors (clusters 3, 7, 8, and 11). Non-progenitor cells in clusters 3 and 8 lacking *Pparg* expression, a marker of committed preadipocytes,[30] were classified as immature preadipocytes, notably containing 99% of inguinal undefined group 5 cells. Cells in cluster 7, characterized by committed preadipocyte and undefined group 3 identities, represented committed preadipocytes, whereas heterogeneous clusters 9 and 11 were excluded from this conservative downstream classification.

To gain deeper molecular insights into these APC states, we conducted multiome sequencing, simultaneously profiling transcriptomic and chromatin accessibility. ChromVAR[35] analysis identified distinct transcription factor (TF) motif enrichments among progenitors, immature preadipocytes, and committed preadipocytes. Specifically, we observed differential motif enrichment for key adipogenic regulators, highlighting distinct regulatory states: immature preadipocytes displayed enrichment for MEIS TF motifs—consistent with Meis1's known role as a negative regulator whose inactivation is required for adipogenesis[36]—while committed preadipocytes showed prominent enrichment of PPAR TF motifs[14,30] (Figures 2D and S2D; Table S1). These observations reinforce that immature preadipocytes represent a distinct cellular population with unique regulatory characteristics.

Altogether, our single-cell data recapitulated two major APC populations: heterogeneous progenitors (clusters 0, 1, 2, 4, 5, 6, 9, and 10 expressing *Dpp4*, *Akr1c18*, and *Smpd3*) and preadipocytes (clusters 3, 7, 8, and 11 expressing *Icam1* and *Cd9*; Figure 2C). Cluster 7 included a small subset expressing *Fabp4* and *Pparg*, markers of committed preadipocytes[14,30] (Figures 2C and S2E). Broad *F3* expression observed across multiple clusters (Figure S1J) contrasts previous reports of restricted *F3* expression,[14] highlighting depot-specific differences and unresolved questions about the adipogenic role of *F3*-expressing cells.[13,14]

Collectively, these analyses recapitulate known APC populations while clearly identifying and characterizing a previously unappreciated immature preadipocyte population. The substantial depot-specific differences in APC identities and proportions, particularly regarding the enriched undefined group 5 population in the skin, underscore unique depot-specific mechanisms governing adipogenesis.

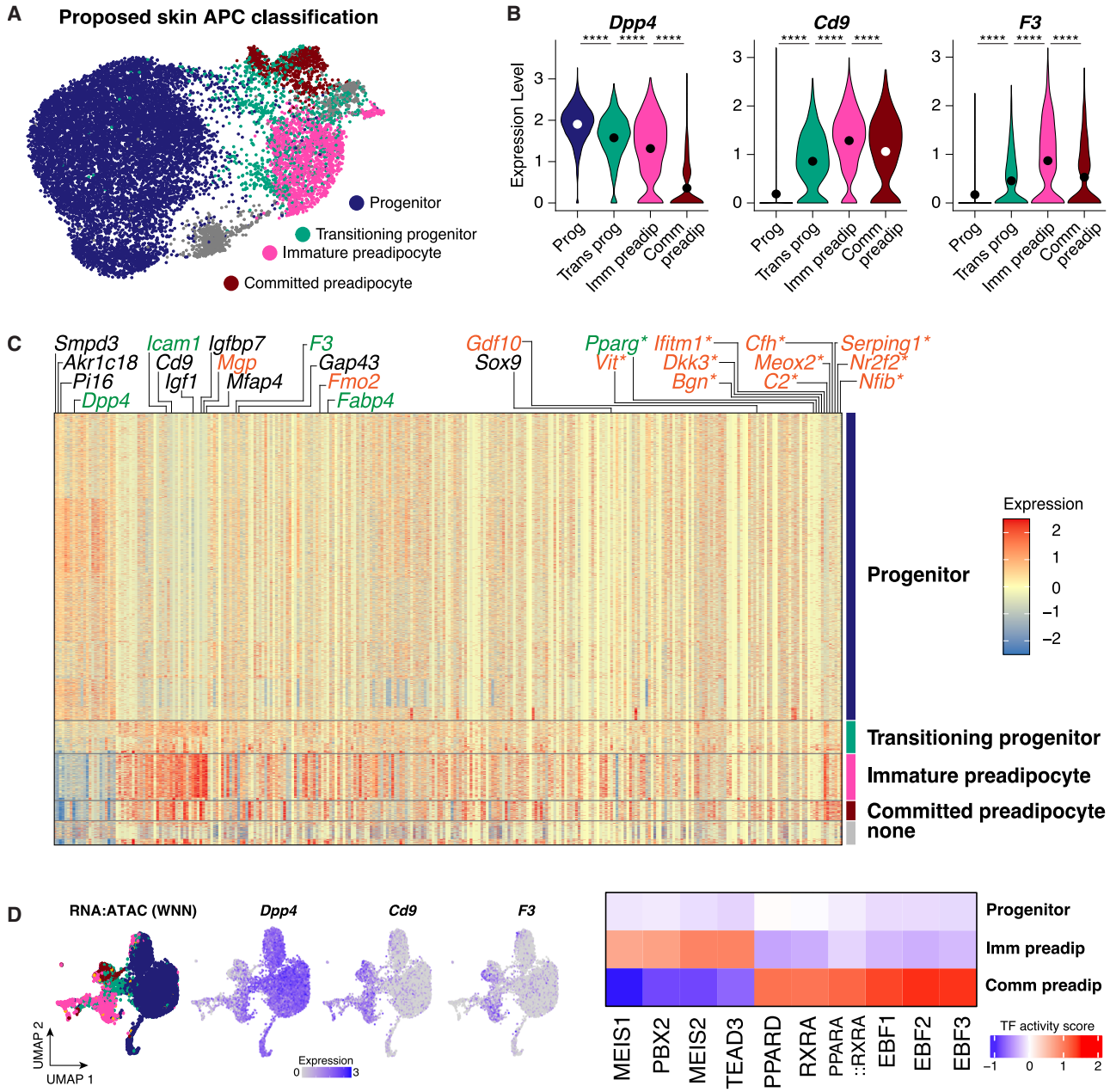

Figure 2. Molecular characterization of adipocyte precursor cell identities in mouse skin

(A) Proposed adipocyte precursor cell (APC) classification in skin.

(B) Expression gradients for *Dpp4*, *Cd9*, and *F3* in classified APCs (****$p < 0.0001$, unpaired t test with Welch's correction).

(C) Heatmap showing differentially expressed genes by cell type. Green gene names indicate known APC markers, and orange gene names correspond to markers previously used to identify group 3 cells. (*) marks features not significantly differentially expressed.

(D) Multiome (RNA and ATAC-seq) weighted nearest neighbors (WNNs) co-embedding and chromVAR TF activity scores at P21 for progenitor, immature preadipocyte, and committed preadipocyte populations (n = 8,279 cells).

See also Figure S2 and Table S1.

Enrichment and functional characterization of skin APC populations

To evaluate the adipogenic potential of our identified skin APC populations, we devised a FACS-based isolation strategy guided by the gradients of *Dpp4* and *Cd9* expression observed in our scRNA-seq analysis (Figures 2B and 3A). This approach allowed us to enrich progenitors (DPP4^{high}) and preadipocyte populations marked by high CD9 expression. Flow cytometry revealed a clear progenitor population characterized by high DPP4 and low CD9 expression (DPP4^{high}/CD9^{low}), along with a continuum of CD9^{high} preadipocytes displaying variable DPP4 expression (Figure S3A). Further separation of these CD9^{high}

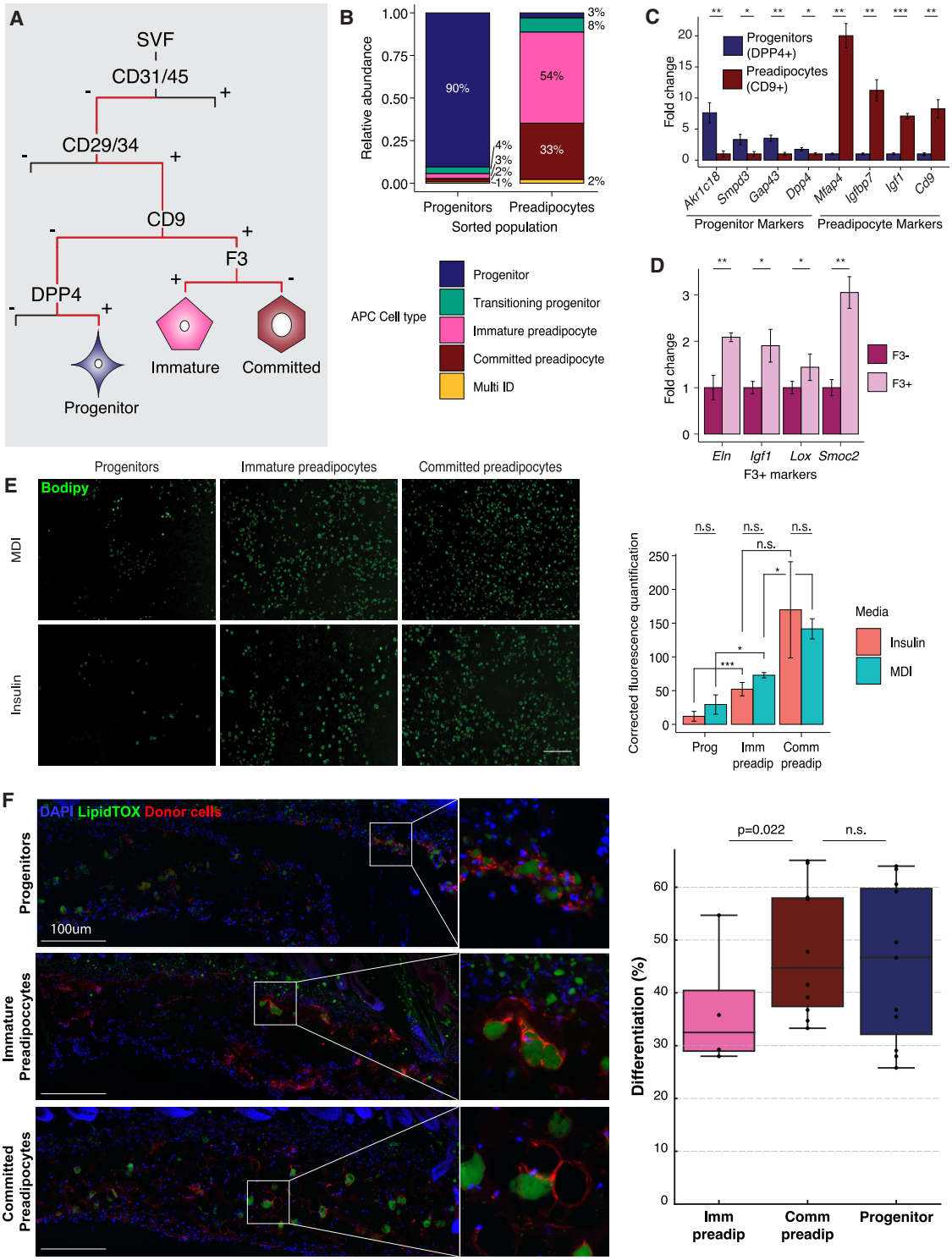

Figure 3. Identification and validation of immature preadipocytes

(A) FACS sorting strategy for isolating APC populations from the stromal vascular fraction (SVF).

(B) scRNA-seq and Capybara classification of FACS-isolated progenitor and preadipocyte populations.

(C) Marker gene expression analysis of sorted progenitors, immature preadipocytes (undefined group 5), and committed preadipocytes (undefined group 3) by qPCR ($n = 3$ biological replicates, unpaired t test with Welch's correction; $^{***}p < 0.001$, $^{**}p < 0.01$, and $^{*}p < 0.05$).

(D) qPCR quantification of mature adipocyte-specific gene expression in immature and committed preadipocytes ($n = 3$ biological replicates, unpaired t test with Welch's correction; $^{**}p < 0.01$ and $^{*}p < 0.05$).

(legend continued on next page)

preadipocytes based on F3 protein expression distinguished immature preadipocytes ($CD9^{high}/F3^{high}$) from committed preadipocytes ($CD9^{high}/F3^{low}$; Figure S3A).

Comparing our strategy to a classically used scheme,[14] we observed that F3+ cells exhibited low ICAM1 expression (Figure S3B). CD9 overlapped significantly with ICAM1 (94%), validating CD9 as a preadipocyte marker. Progenitors isolated using our method lacked high ICAM1 expression, confirming population purity (Figure S3B). Crucially, scRNA-seq with Capybara-based classification and orthogonal qPCR validation confirmed correct enrichment and expression of population-specific markers (Figures 3B–3D).

We functionally characterized isolated progenitors, immature preadipocytes (previously undefined group 5), and committed preadipocytes using *in vitro* and *in vivo* assays. In replating assays, immature preadipocytes demonstrated an increased capacity to expand cell numbers in the short term, whereas committed preadipocytes rapidly lost renewal potential (Figure S3C). Adipogenic differentiation assays demonstrated progenitors had low adipogenic potential, immature preadipocytes showed intermediate differentiation capacity, and committed preadipocytes exhibited the highest differentiation efficiency (Figures 3E and S3D).

By contrast, transplantation *in vivo* revealed robust adipogenic potential for both progenitors and committed preadipocytes, with immature preadipocytes contributing less frequently to mature adipocytes (Figure 3F). These discrepancies suggest that microenvironmental factors enhance progenitor differentiation but limit immature preadipocyte integration into the adipogenic niche. Collectively, these results confirm adipogenic potential across isolated populations, notably demonstrating that immature preadipocytes represent a distinct intermediate population with unique molecular regulation and biological characteristics.

Lineage tracing highlights complex APC hierarchy and differentiation potential in the skin

While committed preadipocytes and undefined group 3 cells originate from progenitors in inguinal adipose depots,[14] the source of immature preadipocytes in skin adipose is unclear. We hypothesized that immature preadipocytes stem from progenitors. However, traditional lineage-tracing approaches using markers such as *Pdgfra*,[24,30,37] *Dpp4*,[38] or *Dlk1(Pref1)*[14] could not specifically distinguish progenitor populations due to overlapping expression profiles between different APC populations (Figures 2B and 2C). Thus, we employed the CellTagging genetic barcoding technique developed by our group,[26,29] which simultaneously captures single-cell transcriptomes and lineage information.

Using CellTagging, we separately labeled progenitors and a mixed preadipocyte population from P21 mouse skin, enriched by our FACS-based strategy, with distinct barcode libraries. We also incorporated a dominant-negative form of Cebpa (DN-Cebpa) to inhibit terminal adipogenesis,[39] enabling clear assessment of differentiation potentials without terminal differentiation influencing the outcome in our competitive transplant setting (Figure 4A). Labeled progenitor and preadipocyte cells were then mixed in physiological proportions and transplanted into the skin of P21 mice during the telogen phase. After 11–13 days, corresponding to the anagen phase onset when adipogenesis increases (around P32),[4] GFP-positive transplanted cells and GFP-negative host APCs were isolated and subjected to scRNA-seq analysis. After quality filtering, we analyzed 19,435 APCs from four independent biological replicates, comprising 10,590 (54.4%) host cells and 8,845 (45.5%) transplanted cells (Figuress 4B, 4C, and S4A). APCs were identified based on mesenchymal markers and *Cd34/Itgb1* co-expression,[24,40] excluding other cell types using marker-based filtering (Table S2).

Using Capybara classification, we identified cell states corresponding to adipocyte progenitors, transitioning progenitors, immature preadipocytes, committed preadipocytes, and multi-ID transitional states (P21 skin dataset as reference; Figure 4D). Between P21 and P32, progenitor cell proportions decreased, shifting toward more committed preadipocyte states, likely reflecting normal postnatal adipogenesis[24] (Figure S4B). Further analysis revealed distinct differentiation patterns based on cellular origin. Progenitor-originating cells differentiated into both immature preadipocytes (31% ± 12%) and committed preadipocytes (33% ± 9%), with a subset maintaining progenitor characteristics (30% ± 12%) (Figure 4E, left). By contrast, preadipocyte-originating cells largely remained or generated a high proportion of immature preadipocytes (56% ± 12%) and produced fewer committed preadipocytes (23% ± 10%) (Figure 4E, right). This indicates progenitors as a significant source of immature preadipocytes and emphasizes their higher potential to form committed preadipocytes compared with preadipocyte-originating cells (33% vs. 23%; $p < 0.0001$, randomization test with Bonferroni correction, two-tailed; Figures 4E and S4C).

Jaccard index analyses further supported these distinctions, revealing progenitor-origin cells enriched in clusters 0, 2, and 6, and committed preadipocyte-origin cells enriched in clusters 3 and 9 (Figure S4D). We also observed a modest but statistically significant expansion in progenitor-derived committed preadipocytes compared with host cells (5%; $p < 0.0001$), whereas preadipocyte-derived committed preadipocytes remained stable ($p = 0.7489$; Figure 4F). Control experiments excluding DN-Cebpa demonstrated that this construct did not significantly alter differentiation outcomes (Figures S4E–S4G).

CellTag information allowed us to distinguish between newly generated immature preadipocytes (derived from progenitors) and pre-existing immature preadipocytes. Gene ontology (GO)

(E) Boron-dipyrromethene (BODIPY) lipid staining (green) showing adipogenic differentiation of APC populations treated with methylisobutylxanthine, dexamethasone, and insulin (MDI) (full adipogenic cocktail) or insulin alone (left), and quantification of fluorescence intensity (right; $n = 3$ biological replicates, two-sample t test with Welch's correction).

(F) Left: representative images showing donor-derived transplanted APC populations (Tomato$^+$, red) and newly formed adipocytes (LipidTOX$^+$, green) in recipient mice. Scale bar, 100 μm. Right: differentiation rate quantification using a linear mixed-effects model (LMM), indicating significantly lower differentiation in immature compared with committed preadipocytes ($p = 0.022$), and progenitors showed no significant difference ($p = 0.983$). Data represent 3 biological and 25 technical replicates.

See also Figure S3.

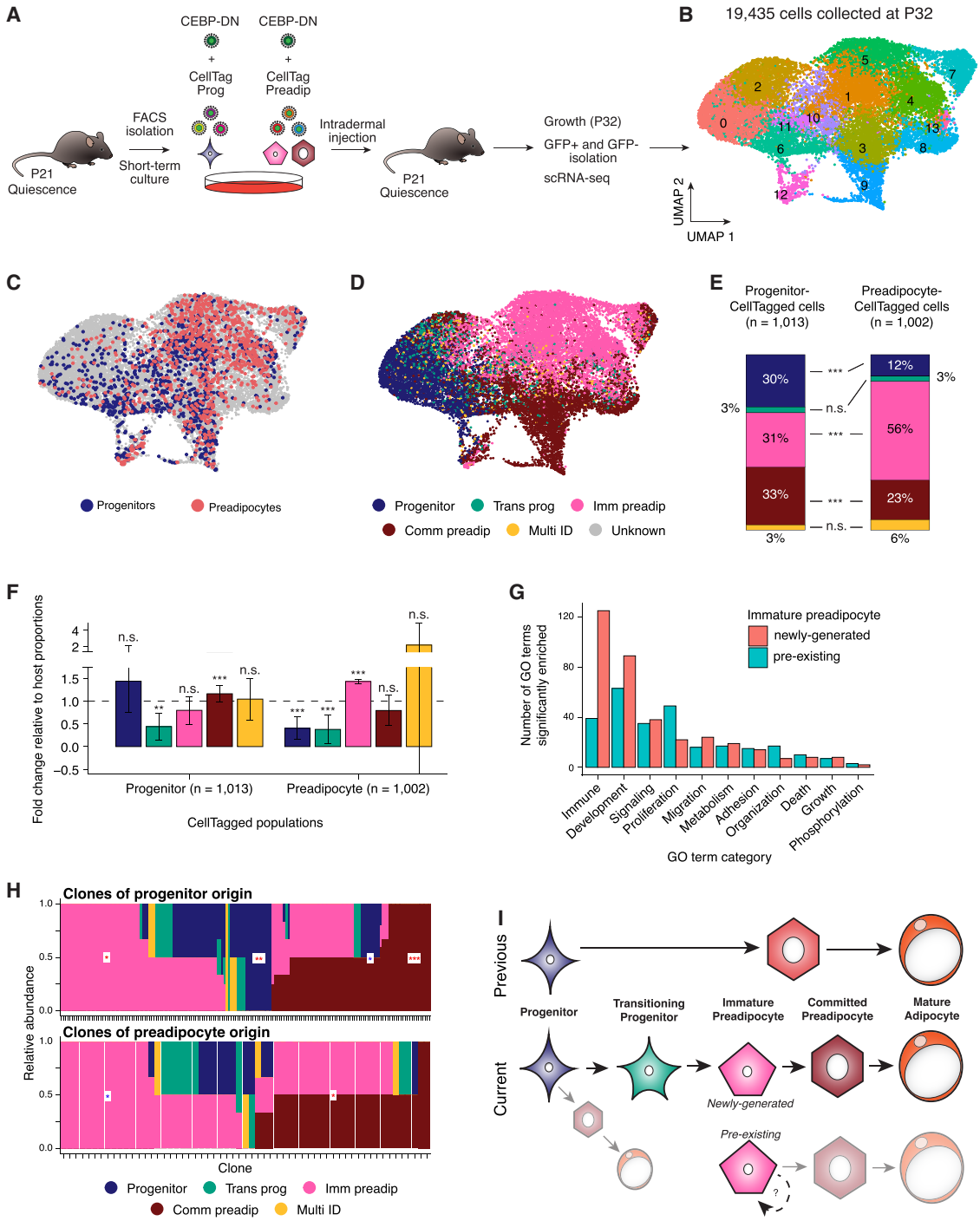

Figure 4. Lineage tracing reveals complex APC hierarchy and differentiation potential

(A) Schematic of *in vivo* lineage tracing competition assay using skin progenitors and pooled immature and committed preadipocytes.

(B) UMAP visualization of 19,435 sequenced APCs from 4 biological replicates (male mice) at P32, after integration and quality control.

(C) UMAP-based identification of transplanted progenitors and preadipocytes via CellTag barcodes in the P32 dataset.

(D) Capybara classification of P32 APCs using the earlier P21 dataset as reference.

(E) Quantification of Capybara cell identities for CellTagged progenitors and preadipocytes (randomization test with Bonferroni correction, two-tailed; ***$p < 0.0001$).

(F) Fold change of cell type proportions relative to host by transplanted cell origin (randomization test with Bonferroni correction, two-tailed; ***$p < 0.0001$ and **$p < 0.001$).

(legend continued on next page)

analysis of differentially expressed genes showed newly generated immature preadipocytes were enriched for proliferation and positive immune regulation pathways and prominently expressed *Shh*, known to promote adipogenic differentiation.[23] By contrast, pre-existing immature preadipocytes exhibited gene expression associated with inhibition of proliferation, notably upregulating *Tnf, Gata3*, and *Pdgfa*, previously reported to inhibit adipogenesis[41–43] (Figures 4G and S4H; Table S2). These differences highlight distinct functional states between newly generated and pre-existing immature preadipocytes.

From these results, we conclude that progenitor-derived cells have greater potential to reach the committed preadipocyte state compared with preadipocyte-derived cells. This finding was unexpected since preadipocytes, given their differentiated phenotype and higher adipogenic potential *in vitro*,[14] were anticipated to more readily become committed preadipocytes. However, our data show that progenitor-derived cells are more efficient at generating committed preadipocytes *in vivo*. These observations suggest distinct differentiation potentials for progenitors and preadipocytes: progenitors may represent a privileged state capable of efficiently producing committed preadipocytes, whereas pre-existing preadipocytes might possess self-renewing properties, independently maintained without relying heavily on progenitor input.

Finally, our transplant studies raise an alternative to the linear model of adipogenesis, in which progenitors sequentially progress through immature and committed preadipocyte states. The reduced potential of immature preadipocytes to generate committed preadipocytes suggests that the lineage may not require passage through an immature state. Instead, progenitors might directly differentiate into committed preadipocytes, while immature preadipocytes may represent a separate, parallel lineage specific to the skin. To test this alternative differentiation model, we leveraged clonal relationships encoded by CellTag sequences. We categorized clones as either "biased" (>50% one cell type) or "split" (50% two cell types). Randomization tests indicated a depletion of split clones directly connecting progenitors and committed preadipocytes (Table S3), suggesting direct differentiation from progenitors to committed preadipocytes is not predominant (Figures 4H and 4I). Collectively, our lineage-tracing data provide insights into skin adipogenesis, highlighting progenitors as major contributors to immature and committed preadipocyte populations. Furthermore, our findings challenge traditional linear differentiation models, suggesting complex, parallel differentiation trajectories and potential depot-specific regulatory mechanisms.

Sox9 is a crucial regulator of the adipocyte progenitor-to-preadipocyte transition

To identify molecular regulators governing progenitor commitment in skin adipogenesis, we sought to explore depot-specific regulatory factors that have been largely overlooked in skin APCs. Although critical TFs and signaling pathways controlling adipogenic lineage commitment have been defined in various *in vitro* models and adipose tissue depots—including *Bmp2* and *Bmp4* in embryonic fibroblast-derived C3H10T1/2 cells[44,45] and depot-specific roles for *Zfp423* and *Sox4*[2,46,47]—the mechanisms specific to skin APCs remain poorly understood. Given the distinct differentiation dynamics we observed, identifying skin-specific adipogenic regulators is essential for comprehensively understanding adipose biology.

Our detailed lineage-tracing approach revealed complex cellular heterogeneity and defined clear differentiation trajectories. This highly quantitative characterization provided an ideal framework for mechanistically dissecting gene regulation in skin adipogenesis. We employed CellOracle, our computational approach, to infer gene regulatory networks (GRNs) from our scRNA-seq data and systematically simulate TF perturbations, enabling unbiased *in silico* prioritization of potential differentiation regulators.[48] We previously demonstrated CellOracle's efficacy in pinpointing key regulators of cell fate decisions across diverse contexts, including zebrafish embryogenesis, mammalian cell lineage reprogramming, and cardiac recovery.[48]

Using CellOracle, we analyzed factors critical for adipogenic commitment by systematically simulating knockout (KO) or upregulation of 165 TFs identified in our skin adipose GRNs. For this analysis, our P32 dataset (Figure 4B) was reprocessed with Monocle2[49] to establish a pseudotime differentiation trajectory rooted in progenitors, accurately reflecting known biological transitions from progenitor-to-preadipocyte states (Figures S5A–S5D, 5A, and 5B). CellOracle produced vector fields representing predicted identity shifts following TF perturbation, summarized into "perturbation scores"[48,50] that indicated whether TF manipulation promoted or inhibited differentiation (STAR Methods; Figures 5C–5E).

Ranking TFs based on these scores identified several known adipogenic regulators among the top candidates, including *Id2, Zbtb7c*, and *Nr4a2*.[51–53] Several other TFs on this list are implicated in adipogenesis but have not been studied in this specific context.[47,52,54] *Sox9* emerged as the highest-ranked TF, with KO simulations predicting inhibited differentiation toward committed preadipocytes and upregulation simulations promoting differentiation into committed preadipocyte states (Figures 5E and S5E). Simulated cell density analyses further supported *Sox9* as a critical positive regulator of adipocyte progenitor differentiation (Figures 5F and S5F–S5I). Positive control simulations with *Id2, Zbtb7c*, and *Nr4a2*[49,51,55] produced similar differentiation outcomes, supporting our *Sox9* findings (Figure S5J). Together, our computational analyses identified *Sox9* as a crucial TF governing progenitor-to-preadipocyte transition, specifically in skin adipogenesis, highlighting unique depot-specific regulatory mechanisms.

(G) GO term enrichment comparing newly generated vs. pre-existing immature preadipocytes.
(H) Cell type composition of clones (≥2 cells per clone) originating from progenitors (top, $n = 168$) or preadipocytes (bottom, $n = 59$). Red asterisks: significant enrichment; blue asterisks; significant depletion. ***$p < 0.001$ and **$p < 0.01$ and *$p < 0.05$.
(I) Comparison of previous (top) and proposed (bottom) differentiation models, highlighting increased potential of progenitors toward committed preadipocytes, whereas pre-existing preadipocytes exhibit limited differentiation potential.
See also Figure S4 and Tables S2 and S3.

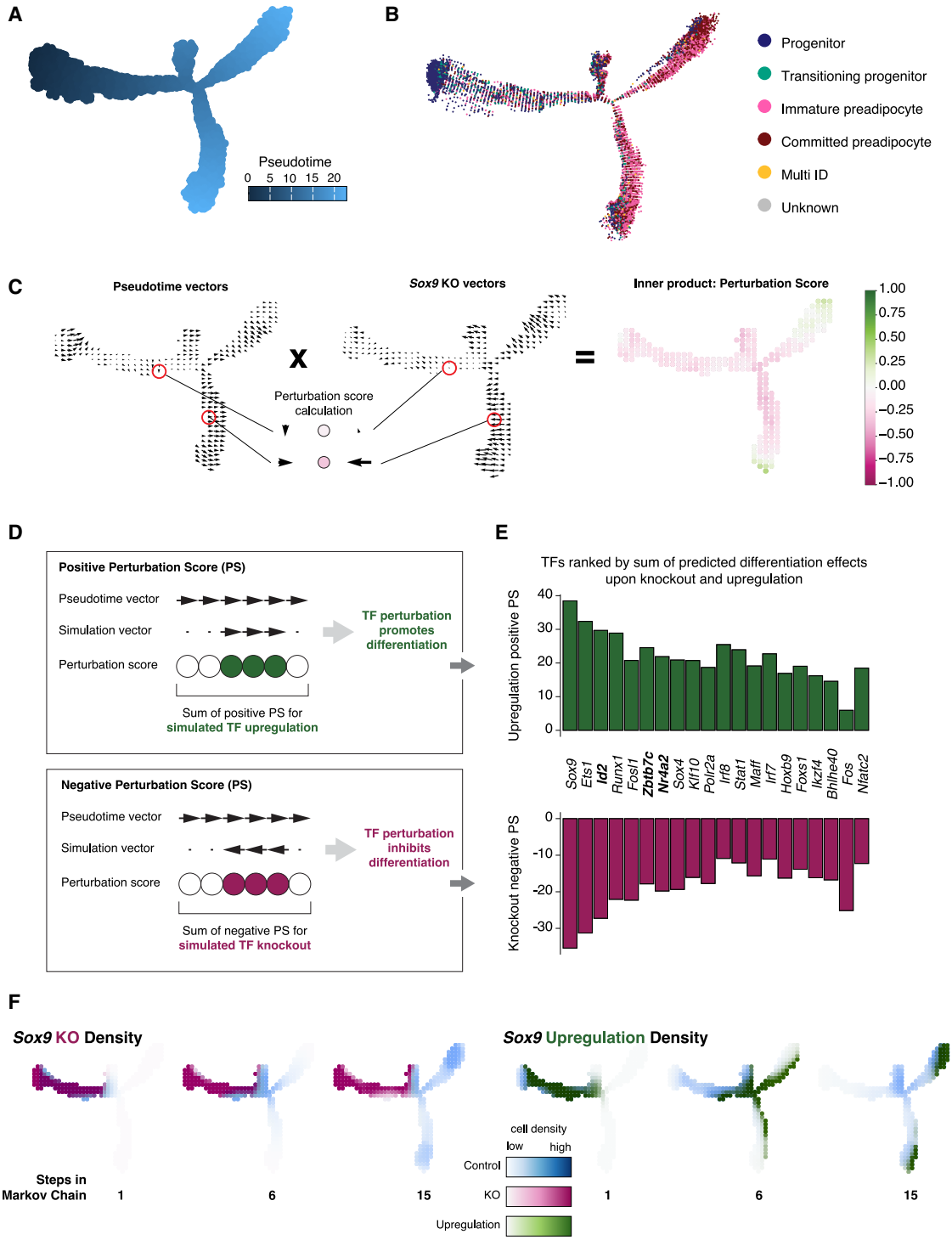

Figure 5. *In silico* prioritization of Sox9 as a regulator of progenitor differentiation

(A) Monocle2 pseudotime overlaid on DDRTree embedding of the P32 dataset, rooted at the highest progenitor density.

(B) Capybara classification of cell types within the Monocle2 embedding.

(C) CellOracle perturbation methodology: pseudotime gradient vector field (left), perturbation simulation vector field (*Sox9* KO example, center), and calculated perturbation score (PS) as their inner product (right).

(D) Schematic illustrating PS interpretation: negative PS indicates inhibited APC differentiation, while positive PS indicates promoted differentiation.

(legend continued on next page)

Sox9 loss-of-function attenuates skin progenitor proliferation and adipogenesis

Our CellOracle simulations prioritized Sox9 as a potential regulator of progenitor-to-preadipocyte transition,[36,56–58] prompting us to experimentally validate this candidate. Further, this prediction contradicted previous reports that *Sox9* KO promotes adipogenesis. Gulyaeva[36] et al. used a Pref1rtTA-Cre model to excise *Sox9 in vivo* and *in vitro*. Isolation and differentiation of the stromal vascular fraction (SVF) from these mice showed increased expression of mature adipocyte markers (*Cebpa*, *Pparg*, and *Plin1*) in *Sox9* KO cells compared with controls.[36] However, this previous study targeted *Sox9* KO to *Dlk1*-expressing cells, representing mainly committed preadipocytes (Merrick et al.[14] and Figure S6A). It is crucial to distinguish that we profiled cells at earlier stages of the differentiation process, in which our CellOracle simulations focused on progenitor and preadipocyte transitions. At these stages, *Sox9* expression is gradually upregulated (Figure S5F).

To test the role of Sox9 in skin adipogenesis, we crossed *Sox9*$^{flox/flox}$ mice with *Pdgfra*CreER; mTmG mice, enabling lineage tracing of PDGFRa+ APCs following tamoxifen administration at P18. Quantifying newly generated GFP+ adipocytes in these mice revealed significantly reduced adipocyte formation upon *Sox9* KO compared with controls (Figure 6A), supporting a positive role for Sox9 in adipocyte differentiation *in vivo*.

To dissect the role of Sox9 specifically in progenitors, we isolated these cells and transduced them with lentiviruses encoding either *Sox9* short hairpin RNA (shRNA) (achieving ~98% knockdown, $p = 9.748 \times 10^{-5}$, Figure S6B), scrambled shRNA control, or *Sox9* overexpression (OE) constructs. These populations were mixed equally and transplanted into mouse skin at P21 and recovered for scRNA-seq 11 days later (Figure 6B). Sox9-OE cells exhibited strong competitive advantages, vastly outnumbering Sox9-KD and control cells, suggesting a critical role for Sox9 in progenitor cell fitness and survival (Table S4).

To confirm and clarify this effect, we separately transplanted *Sox9*-shRNA-treated or control shRNA-treated progenitors into mouse skin. *Sox9* KD significantly decreased the number of recovered progenitors (0.5-fold, $p = 0.047$; Figure 6C). Furthermore, *in vitro* EdU proliferation assays demonstrated significantly lower proliferation rates in progenitors (0.22-fold, $p = 6.224 \times 10^{-4}$) and preadipocytes (0.01-fold, $p = 1.627 \times 10^{-4}$) following *Sox9* KD (Figures 6D and S6C). *Sox9* KD also increased apoptosis in progenitors and preadipocytes ($p = 0.028$ and $p = 0.048$, respectively; Figure S5D). Finally, *Sox9* KD in both APC populations resulted in markedly reduced expression of terminal adipocyte differentiation markers and lower intracellular lipid accumulation during *in vitro* differentiation assays (Figures 6E–6G). These results validate our computational predictions, establishing Sox9 as a critical regulator that promotes progenitor and preadipocyte proliferation, survival, and differentiation during skin adipogenesis.

Sox9 OE promotes progenitor cycling and transition to preadipocytes

Our perturbation experiments and competitive transplants revealed a critical role for Sox9 in both proliferation and differentiation of adipocyte progenitors and preadipocytes. The shift from proliferation to differentiation in adipogenesis involves coordinated regulation between cell cycle and differentiation factors, initiating progenitor commitment.[59] While *Sox9* KD inhibited proliferation, *Sox9* OE significantly increased EdU incorporation in progenitors compared with control (1.15-fold increase, $p = 0.01043$; Figures 6D and S6C). Additionally, CellOracle predicted accelerated differentiation upon physiological-level *Sox9* upregulation, prompting further investigation.

Analyzing our competitive transplant dataset (Figure 6B), comprising 2,467 Sox9-OE cells, we classified cell identities using Capybara, referencing our P21 dataset (Figure 2A). We found significant enrichment of immature and committed preadipocytes and a corresponding depletion of progenitors and transitioning progenitors among Sox9-OE compared with host cells (all comparisons $p < 0.0001$, randomization test with Bonferroni correction; Figure 6H). Overall, differentiated preadipocytes accounted for 85% of *Sox9* OE vs. 53% of host cells. Comparison of Sox9-OE progenitors to progenitors from our P32 dataset (Figure 4) further confirmed fewer progenitors and increased committed preadipocytes in Sox9-OE populations ($p < 0.0001$; Figure 6I), supported by *in vitro* flow cytometry (Figures S6E–S6H). *Sox9* OE specifically promoted proliferation and differentiation in progenitors rather than preadipocytes (Figures 6D and S6I–S6K). These results align with CellOracle predictions, underscoring Sox9's role in progenitor differentiation toward preadipocytes.

Mechanistically, RNA-seq of Sox9-OE vs. control progenitors identified 138 significantly enriched genes also elevated in naive preadipocytes at P32 compared with progenitors (Table S4). GO and pathway analyses highlighted enriched terms related to proliferation and cell cycle activation (Figure 6J; Table S4), aligning with our network analyses that identified several Sox9-targeted cell cycle regulators in progenitors (Table S4).

Our results highlight the strong association between precursor proliferation and adipogenic differentiation,[20,23,24] showing that Sox9 directly enhances proliferative capacity to facilitate differentiation. Specifically, loss of *Sox9* impaired both proliferation and differentiation, whereas *Sox9* OE accelerated these processes in progenitors. Together with prior evidence that Sox9 inhibits terminal differentiation,[36] our findings indicate a model in which Sox9 drives adipocyte precursor expansion and lineage commitment, and its subsequent downregulation is essential for cell cycle exit and terminal differentiation into mature adipocytes.

Intrinsic and extrinsic factors influencing skin progenitor differentiation

In this study, we comprehensively characterized APCs in skin adipose tissue and identified intrinsic factors regulating their

(E) Perturbation scores of the top 20 transcription factors (TFs) ranked by CellOracle; knockout (magenta, left) and upregulation (green, right).
(F) Markov simulations showing predicted cell density shifts after *Sox9* perturbation. Density plots for *Sox9* KO (magenta, left) and *Sox9* OE (green, right) overlaid on combined pseudotime gradient and randomized vector field simulations (blue), illustrating changes at 1, 6, and 15 Markov chain steps.
See also Figure S5.

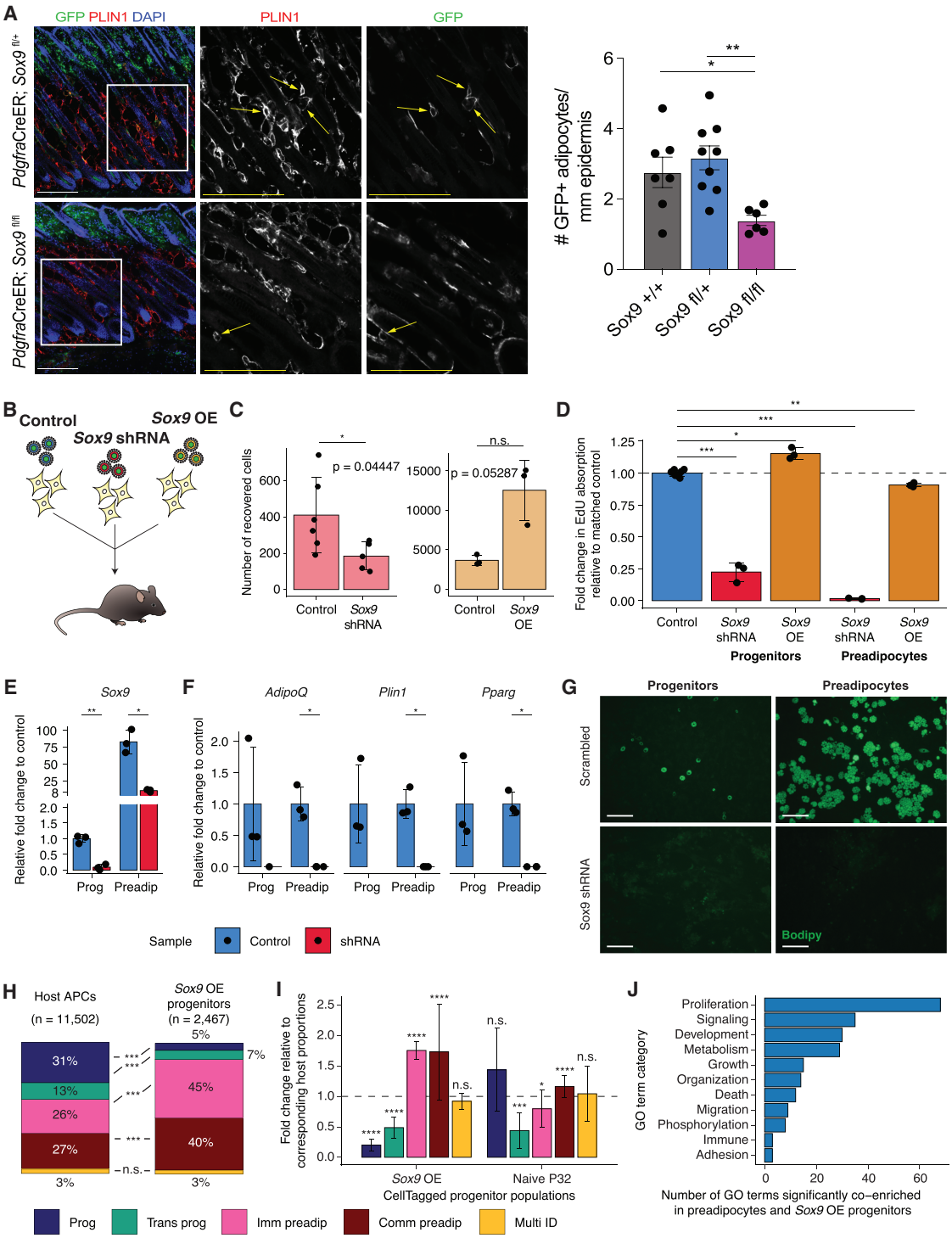

Figure 6. Experimental validation of Sox9 as a regulator of APC differentiation

(A) Lineage tracing of PDGFRA$^+$ APCs in *Pdgfra*CreER; mTmG; *Sox9*$^{flox/flox}$ mice treated with tamoxifen at P18 shows reduced GFP$^+$ adipocyte formation compared with *Sox9*$^{+/+}$ and *Sox9*$^{flox/+}$ controls (n = 6–9 biological replicates; one-way ANOVA). Scale bar, 250 μm.

(B) Schematic of *Sox9* overexpression/knockdown (OE/KD) experiment in progenitors isolated from mice.

(C) Total APCs recovered post-transplantation of Sox9-KD and Sox9-OE progenitors (unpaired t test with Welch's correction, two-tailed; *$p < 0.05$).

(D) Fold change of EdU-positive APCs in Sox9-KD, -OE, and controls (n = 3 biological replicates; unpaired t test, two-tailed; ***$p < 0.001$, **$p < 0.01$, and *$p < 0.05$).

(E) *Sox9* qPCR expression on day 8 post-lentiviral transduction with scrambled or *Sox9* shRNA (n = 3 biological replicates; unpaired t test, two-tailed; **$p < 0.01$ and *$p < 0.05$).

(legend continued on next page)

differentiation transitions. To further dissect the roles of intrinsic and extrinsic influences on progenitor differentiation, we conducted cross-depot transplantation experiments. Previous studies present conflicting evidence regarding niche influence: transplantation of subcutaneous cells into visceral adipose depots results in transplanted cells adopting functions characteristic of the host environment,[60] whereas other studies suggest intrinsic cellular traits primarily determine differentiation outcomes.[61] However, the latter studies mainly relied on marker expression rather than adipocyte formation. Therefore, coupling cross-depot transplantation with scRNA-seq provided a unique opportunity to rigorously define intrinsic progenitor identities and assess extrinsic niche effects with high resolution.

We transplanted CellTagged skin progenitors into the inguinal fat pad at P21 to specifically investigate the impact of the microenvironment on differentiation potential (Figure 7A). We selected the inguinal depot for these experiments because it shares several cellular and molecular characteristics with skin adipose tissue (Figure 1) yet notably differs in cell type proportions and adipogenic dynamics. This combination of similarities and differences between depots provided an ideal system to rigorously assess extrinsic environmental influences while controlling for intrinsic progenitor properties. At approximately P32, transplanted GFP+ progenitors and host inguinal progenitors (LIN- cells) were isolated via FACS, yielding 1,609 transplanted and 19,842 host cells from two biological replicates (Figures 7B and 7C). Using Capybara analysis referencing our established P21 skin dataset, we classified and compared cell identities between transplanted and host populations (Figure 7D).

Host inguinal APC identities primarily comprised progenitors (56.3% ± 0.1%), transitioning progenitors (17.1% ± 0.2%), and committed preadipocytes (19% ± 1%), with immature preadipocytes representing a smaller proportion (6% ± 1%), consistent with previous findings.[14] By contrast, transplanted skin progenitors showed distinct distributions: notably higher proportions of immature preadipocytes (31% ± 4%) and transitioning progenitors (29.4% ± 0.5%), fewer progenitors (30.9% ± 0.8%), and significantly lower committed preadipocytes (4.8% ± 2.6%; Figure 7D). These findings suggest that the inguinal niche does not fully reprogram skin progenitor identity and potential during the developmental period from P21 to P32.

We further compared progeny arising from skin progenitors transplanted into skin vs. inguinal depots. Committed preadipocytes were significantly more abundant (expanded ~7-fold) in skin-transplanted progenitors (32.9% ± 9.2%) compared with those transplanted into inguinal adipose (4.8% ± 2.6%, $p < 0.0001$). Conversely, transitioning progenitors were significantly depleted in the skin (3.2% ± 2.7%) relative to inguinal transplants (29.4% ± 0.5%, $p < 0.0001$; randomization test with Bonferroni correction; Figure 7D). Similar patterns emerged when comparing transplanted populations to their host tissues (Figure S7A), highlighting the niche's critical role in differentiation, with the skin environment particularly promoting adipogenic commitment. Nonetheless, transplanted skin progenitors retained intrinsic characteristics distinct from host progenitors, confirmed by NN transcriptional similarity analysis (fraction of NN belonging to inguinal host progenitors: 0.78 vs. transplanted skin progenitors: 0.33; $p < 2.2 \times 10^{-16}$; Figure 7E). Skin progenitors transplanted back into the skin environment maintained greater similarity to host progenitors (host progenitors: 0.66, transplanted progenitors: 0.62, $p = 0.026$, Welch's two-sample t test; Figure 7E).

To identify an intrinsic progenitor signature independent of depot environment, we analyzed differentially expressed genes enriched specifically in progenitors vs. preadipocytes at P32, excluding genes differentially expressed between skin and inguinal adipose depots. This approach generated a refined set of 27 genes uniquely representing intrinsic progenitor identity (Figures 7F–7H and S7B). Notably, these genes include known regulators and markers of adipocyte differentiation and mesenchymal progenitor populations, such as *Akr1c18*, *Dpp4*, *Gap43*, *Pi16*, and *Wnt2* (Figure 7H; Table S5).

To further validate the specificity of this intrinsic gene signature, we analyzed its enrichment in a comprehensive fibroblast atlas spanning 16 tissues, which also includes mesenchymal populations with adipogenic potential.[32] This intrinsic signature was prominently enriched within fibroblast populations from skin and subcutaneous adipose tissues, particularly within a previously identified Pi16+ fibroblast cluster representing highly progenitor-like states (Figures 7I and 7J). Notably, the Pi16+ cluster comprises populations mainly from the skin or subcutaneous adipose (Figure S7C). Together, these observations suggest that the progenitors in the skin and subcutaneous tissues may be more similar to one another than to those in the visceral depot. This result correlates well with recent findings suggesting intrinsic differences between inguinal and visceral progenitors.[61]

Finally, to understand how extrinsic niche factors influence skin progenitor differentiation, we compared gene expression profiles between skin progenitors transplanted into skin or inguinal depots. Skin-transplanted progenitors exhibited elevated immune response and inflammatory activity signatures (Figure 7K; Table S6), consistent with inflammation's known role in facilitating adipogenesis and tissue remodeling.[62] By contrast, progenitors transplanted into inguinal adipose showed enriched expression of developmental, signaling, and proliferation-associated pathways, including PDGF and alpha-adrenergic receptor signaling (Table S6). These pathways are known to promote progenitor proliferation and maintenance, correlating with limited differentiation into committed preadipocytes observed in inguinal environments.[24,63]

(F) Mature adipocyte gene expression by qPCR on day 8 post-transduction ($n = 3$ biological replicates; unpaired t test, two-tailed; $^{*}p < 0.05$; NA indicates below detection).
(G) Representative BODIPY staining images on day 8 of differentiation post-transduction. Scale bar, 200 μm.
(H) Capybara identity proportions of host and Sox9-OE progenitors based on P21 identities (randomization test, Bonferroni correction; $^{***}p < 0.0001$).
(I) Fold change in cell type proportions comparing Sox9-OE progenitors at P32 to host cells (randomization test, Bonferroni correction; $^{***}p < 0.0001$ and $^{**}p < 0.001$).
(J) GO terms enriched in both preadipocyte vs. progenitor populations at P32 and Sox9-OE progenitors relative to controls after 48 h *in vitro* culture.
See also Figure S6 and Table S4.

CellPress
OPEN ACCESS

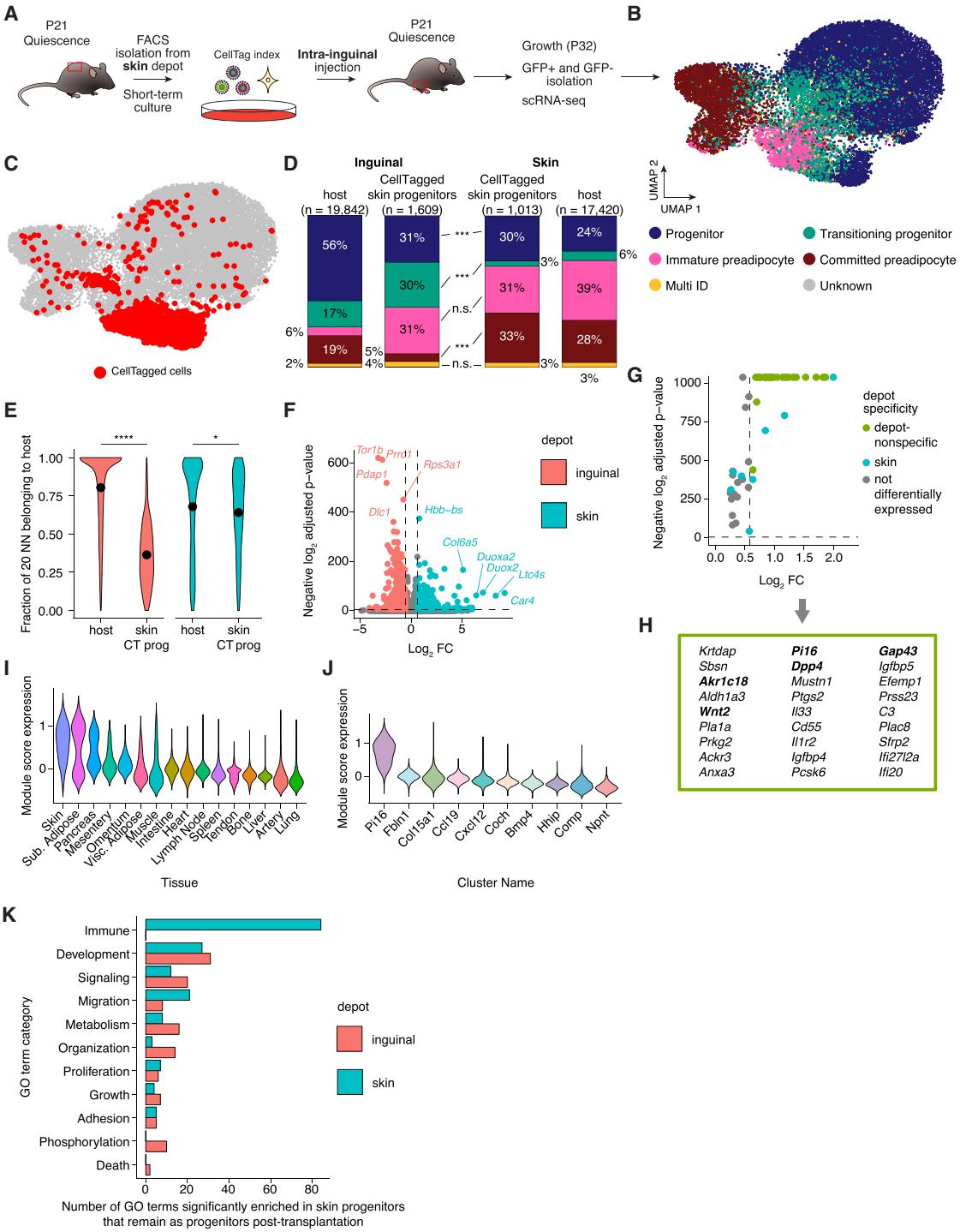

Figure 7. Skin progenitors maintain intrinsic identity yet respond to inguinal niche cues

(A) Schematic of cross-depot transplantation of CellTagged skin progenitors followed by scRNA-seq.

(B) UMAP visualization of 21,451 APCs from inguinal tissue, classified by Capybara using the P21 skin dataset as reference ($n = 3$ biological replicates; male mice).

(C) Identification of transplanted skin progenitors by CellTag barcode in UMAP embedding.

(D) Fold change in cell type proportions of skin progenitors transplanted into inguinal vs. skin tissue, relative to host proportions, normalized to skin transplants (randomization test with Bonferroni correction, two-tailed; ***$p < 0.0001$).

(E) Fraction of NNs classified as progenitors within respective host tissues (unpaired t test with Welch's correction, two-tailed; ****$p < 0.0001$ and *$p < 0.05$).

(F) Differentially expressed genes in skin progenitors transplanted into inguinal or skin adipose depots (>1.5-fold change, adjusted $p < 0.05$, Bonferroni correction).

(legend continued on next page)

Together, these findings demonstrate that a combination of stable cell-intrinsic characteristics and the cell-extrinsic niche dictates the identity and potential of skin progenitors. Crucially, the environment likely dictates the rate of adipogenesis, where we posit that the rapid adipogenesis we observe in the skin is required for the active turnover of this depot relative to the more dormant inguinal depot.

DISCUSSION

In this study, we characterized a previously unrecognized immature preadipocyte population in skin adipose tissue and elucidated distinct differentiation potentials between progenitors and preadipocytes. We identified Sox9 as a critical regulator promoting progenitor differentiation into both immature and committed preadipocytes and demonstrated its role in APC proliferation. Additionally, we examined the influence of the cellular niche on progenitor differentiation, identifying a niche-independent gene signature specific to skin progenitors.

While single-cell approaches have previously clarified fibroblast and adipocyte precursor biology during skin homeostasis, disease, and repair,[40,64–67] we combined lineage tracing with computational modeling and experimental perturbations to pinpoint drivers of adipogenic lineage commitment. Our advanced lineage-tracing method, CellTagging, enabled precise targeting of progenitor and preadipocyte populations, allowing direct comparison of differentiation potentials within identical microenvironments.[68]

Our unbiased computational classification approach, leveraging existing single-cell datasets, identified an immature preadipocyte population previously considered non-adipogenic due to their scarcity in inguinal adipose tissue.[14] We demonstrate this population's adipogenic capability and reveal that adipogenesis in skin deviates from the traditional linear differentiation model. Specifically, progenitors primarily produce committed preadipocytes, whereas preexisting preadipocytes persist in distinct immature states. These findings challenge traditional paradigms and suggest potential mechanisms such as preadipocyte self-renewal or selective differentiation from progenitor populations. Supporting the self-renewal hypothesis, preadipocytes actively proliferate following depilation-induced skin injury.[24] Similar maintenance of populations independent of stem-like progenitors has also been reported in hematopoietic and epithelial tissues.[69–71] Furthermore, given progenitors' pronounced capacity for differentiation into committed preadipocytes, it is plausible that both homeostatic and induced (excess-energy) adipogenesis could preferentially promote progenitor or preadipocyte differentiation, depending on specific physiological demands.

Using our defined lineage framework, we employed *in silico* perturbation[48] to prioritize TFs governing APC differentiation, identifying Sox9 as a leading candidate. Our analyses showed gradual *Sox9* upregulation as progenitors transitioned to preadipocyte states. Experimental validation revealed *Sox9* loss impaired proliferation and terminal differentiation in progenitors and preadipocytes, whereas forced *Sox9* expression enhanced progenitor proliferation and differentiation into preadipocytes. Interestingly, *Sox9* OE did not further advance preadipocyte differentiation, indicating a critical threshold of *Sox9* expression.

We propose a model where Sox9 initiates APC cycling and lineage commitment, with subsequent downregulation necessary for cell cycle exit and terminal differentiation into mature adipocytes.[36] This stage-specific Sox9 function mirrors its role in other tissues, such as chondrocyte differentiation,[71] kidney regeneration,[72] and cell fate decisions in the intestine.[73] Our findings underscore the interplay between proliferation and differentiation in adipogenesis, emphasizing Sox9's central role in coupling these processes.[59] The known role of proliferation during adipogenesis, specifically during the phase termed "mitotic clonal expansion," benefits adipogenesis by expanding the population of cells capable of adipogenic commitment.[74] However, cell cycle exit is required for terminal differentiation. Our findings highlight that Sox9 is a crucial TF coupling differentiation to the cell cycle, promoting APC expansion and differentiation while regulating the timing of cell cycle exit and subsequent terminal differentiation.

Finally, we conducted comparative analyses between skin and inguinal adipose depots, highlighting similarities in progenitor characteristics yet significant differences in adipogenic potential and environmental responsiveness.[60,75] Our cross-depot transplantation revealed the environment significantly influences adipogenic differentiation rates. Specifically, skin progenitors transplanted into the inguinal depot generated fewer committed preadipocytes compared with native skin conditions, despite retaining intrinsic transcriptional identity. This suggests the skin's intrinsic population of immature preadipocytes facilitates cyclical mature adipocyte production in response to hair growth,[23,76] whereas committed preadipocytes may primarily address immediate energy storage demands. Understanding these depot-specific differences in adipogenesis can inform therapeutic strategies aimed at enhancing mature adipocyte generation to mitigate hypertrophy-associated complications.[77]

Finally, we compared adipocyte precursors between skin and inguinal adipose depots. Unbiased cell typing revealed many shared cell types between these depots, though in different proportions. While progenitors from both tissues share substantial characteristics, we observed intrinsic differences in adipogenic potential and environmental responsiveness.[60,75] Cross-depot transplantation showed skin progenitors transplanted into inguinal adipose generated fewer committed preadipocytes compared with native skin conditions, despite retaining intrinsic

(G) Identification of 27 genes specifically enriched in progenitor populations across depots (>1.5-fold change, adjusted $p < 0.05$, Bonferroni correction, excluding depot-specific genes).
(H) 27-gene signature representing intrinsic skin progenitor identity.
(I) Module score expression of the intrinsic 27-gene signature across tissues in a fibroblast atlas.[32]
(J) Expression of the 27-gene signature module score across defined clusters in the fibroblast atlas (Buechler et al.[32]).
(K) GO terms enriched among differentially expressed genes between progenitors transplanted into inguinal vs. skin adipose tissue, categorized by specified keywords.
See also Figure S7 and Tables S5 and S6.

transcriptional features. This likely reflects robust, cyclic adipogenic signals in skin linked to hair growth[23,76] vs. predominantly basal adipogenesis in the inguinal depot at this stage.[21,78] Thus, immature preadipocytes in skin may meet cyclical demands for adipogenesis, while committed preadipocytes respond to immediate energy storage needs. Understanding these depot-specific adipogenic mechanisms can inform therapeutic strategies to enhance mature adipocyte production, mitigating hypertrophy-associated adverse effects.[77]

In summary, combining scRNA-seq, computational classification via Capybara, and advanced genetic lineage tracing, we identified and characterized an unrecognized immature preadipocyte population in skin. We established Sox9 as a crucial regulator governing progenitor proliferation and differentiation and described intrinsic and extrinsic determinants shaping adipogenic potential. These insights offer valuable mechanistic understanding and therapeutic opportunities to modulate adipose tissue dynamics, mature adipocyte generation, and associated inflammatory conditions.[5]

Limitations of the study

Our approach of isolating and transplanting skin adipose cells could introduce variables absent in native adipogenesis. Nonetheless, it remains the most precise available strategy to specifically target progenitor and preadipocyte populations, consistent with prior studies.[14] Due to limited efficiency in recovering CellTag barcodes via snRNA-seq, we relied on *in vivo* transplantation assays rather than direct tracking of mature adipocyte formation. Further spatial validation using immunofluorescence could offer additional insights, although distinguishing adipocyte precursors from fibroblasts remains technically challenging. To classify cell identity in dynamic differentiation contexts such as adipogenesis, we applied Capybara, a method specifically designed for this purpose and previously demonstrated across multiple biological systems.[31] Although independent adoption and benchmarking of Capybara by other groups have so far been limited, such validation will be valuable to confirm its robustness and reproducibility. Here, our findings are additionally supported by complementary computational analyses. Ultimately, future studies employing *in vivo* lineage tracing[79,80] will be essential for comprehensively characterizing native adipocyte precursor differentiation trajectories.

RESOURCE AVAILABILITY

Lead contact

Requests for further information and resources should be directed to and will be fulfilled by the lead contact, Samantha A. Morris, samorris2@bwh.harvard.edu.

Materials availability

CellTag libraries are available via Addgene: https://www.addgene.org/pooled-library/morris-lab-celltag/.

Data and code availability

All raw data are available on GEO at GEO: GSE241627: https://www.ncbi.nlm.nih.gov/geo/query/acc.cgi?acc=GSE241627. Processed single-cell Seurat objects are available at https://tinyurl.com/5et2bh5n. Code for processing and analysis is available at https://github.com/morris-lab/adipogenesis-reproducibility-repo, https://doi.org/10.5281/zenodo.15831916.

ACKNOWLEDGMENTS

We thank members of the Morris laboratory for helpful discussions, the Washington University Center for Cellular Imaging (WUCCI) at Washington University School of Medicine, and the Alvin J. Siteman Cancer Center at Washington University School of Medicine and Barnes-Jewish Hospital in St. Louis, MO, for the use of the Siteman Flow Cytometry, which provided FACS service. This study has been funded by the National Institute of General Medical Sciences R01 GM126112 (S.A.M.); R21 AR077825 (S.A.M.); the Silicon Valley Community Foundation, Chan Zuckerberg Initiative grant DAF2021-238797 (S.A.M.); Allen Distinguished Investigator Award through the Paul G. Allen Frontiers Group (S.A.M.); Vallee Scholar Award (S.A.M.); Sloan Research Fellowship (S.A.M.); New York Stem Cell Foundation Robertson Investigator Award (S.A.M.); Rita Levi-Montalcini Postdoctoral Fellowship from the Center of Regenerative Medicine, Washington University in St. Louis (G.C.R.-G.); NIH-T32HG000045-21 (E.G.B.); and NIGMS- R01GM126112-03S1 supplement (C.E.G.).

AUTHOR CONTRIBUTIONS

Conceptualization: S.A.M. and G.C.R.-G.; methodology: S.A.M., G.C.R.-G., E.G.B., and M.S.R.; experimental procedures: G.C.R.-G., E.G.B., C.E.G., R.L.M., K.K., K.J., V.J., and B.A.S.; data analysis: S.A.M., G.C.R.-G., E.G.B., C.E.G., W.K., K.J., V.J., B.A.S., and M.S.R.; funding acquisition: S.A.M.; writing – original draft: S.A.M., G.C.R.-G., E.G.B., and C.E.G.

DECLARATION OF INTERESTS

S.A.M. and G.C.R.-G. are co-founders of CapyBio Inc. S.A.M. is on the advisory board of *Cell Stem Cell*.

STAR★METHODS

Detailed methods are provided in the online version of this paper and include the following:

- KEY RESOURCES TABLE
- EXPERIMENTAL MODEL AND STUDY PARTICIPANT DETAILS
  - Mice
- METHOD DETAILS
  - Adipocyte Precursor Cell Culture
  - Adipocyte Precursor differentiation
  - Adipocyte Precursor Cell Transplants
  - *In Vivo* Adipocyte Differentiation Potential
  - Proliferation and Annexin staining
  - Immunofluorescence and Tissue Staining
  - RNA Extraction and Real-Time PCR
  - FACS and Analysis
  - CellTag and plasmids
  - Lentivirus production
  - Virus transduction
  - Transplantation Assay for virus-treated cells
  - scRNA-seq and scATAC-seq
  - CellTag amplification for scRNA-seq (CellTag-RNA PCR)
  - Basic data alignment and processing
  - Integration
  - CellTag index extraction
  - Published reference cell type classification
  - Cell type classification by Capybara
  - Differential expression and multiome analysis
  - Jaccard similarities and modified z score procedure
  - CellOracle analysis
  - Randomized testing of enrichment of CellTag populations and cell type classifications
  - Randomized testing for enrichment and depletion of clone types
  - Bodipy staining quantification
- QUANTIFICATION AND STATISTICAL ANALYSIS

SUPPLEMENTAL INFORMATION

Supplemental information can be found online at https://doi.org/10.1016/j.stem.2025.07.004.

Received: June 14, 2024
Revised: March 12, 2025
Accepted: July 10, 2025
Published: July 30, 2025

REFERENCES

1. Zhang, L.J., Guerrero-Juarez, C.F., Hata, T., Bapat, S.P., Ramos, R., Plikus, M.V., and Gallo, R.L. (2015). Innate immunity. Dermal adipocytes protect against invasive *Staphylococcus aureus* skin infection. Science *347*, 67–71. https://doi.org/10.1126/science.1260972.
2. Plikus, M.V., Guerrero-Juarez, C.F., Ito, M., Li, Y.R., Dedhia, P.H., Zheng, Y., Shao, M., Gay, D.L., Ramos, R., Hsi, T.-C., et al. (2017). Regeneration of fat cells from myofibroblasts during wound healing. Science *355*, 748–752. https://doi.org/10.1126/science.aai8792.
3. Shook, B., Rivera Gonzalez, Ebmeier, S., Grisotti, G., Zwick, R., and Horsley, V. (2016). The role of adipocytes in tissue regeneration and stem cell niches.Annu. Rev. Cell Dev. Biol. *32*, 609–631. https://doi.org/10.1146/annurev-cellbio-111315-125426.
4. Festa, E., Fretz, J., Berry, R., Schmidt, B., Rodeheffer, M., Horowitz, M., and Horsley, V. (2011). Adipocyte lineage cells contribute to the skin stem cell niche to drive hair cycling. Cell *146*, 761–771. https://doi.org/10.1016/j.cell.2011.07.019.
5. Shao, M., Vishvanath, L., Busbuso, N.C., Hepler, C., Shan, B., Sharma, A. X., Chen, S., Yu, X., An, Y.A., Zhu, Y., et al. (2018). De novo adipocyte differentiation from Pdgfrβ+ preadipocytes protects against pathologic visceral adipose expansion in obesity. Nat. Commun. *9*. https://doi.org/10.1038/s41467-018-03196-x.
6. Klöting, N., and Blüher, M. (2014). Adipocyte dysfunction, inflammation and metabolic syndrome. Rev. Endocr. Metab. Disord. *15*, 277–287. https://doi.org/10.1007/s11154-014-9301-0.
7. Berry, R., Jeffery, E., and Rodeheffer, M.S. (2014). Weighing in on Adipocyte Precursors. Cell Metab. *19*, 8–20. https://doi.org/10.1016/j.cmet.2013.10.003.
8. Shook, B.A., Wasko, R.R., Mano, O., Rutenberg-Schoenberg, M., Rudolph, M.C., Zirak, B., Rivera-Gonzalez, G.C., López-Giráldez, F., Zarini, S., Rezza, A., et al. (2020). Dermal Adipocyte Lipolysis and Myofibroblast Conversion Are Required for Efficient Skin Repair. Cell Stem Cell *26*, 880–895.e6. https://doi.org/10.1016/j.stem.2020.03.013.
9. Jiang, Y., Berry, D.C., Tang, W., and Graff, J.M. (2014). Independent stem cell lineages regulate adipose organogenesis and adipose homeostasis. Cell Rep. *9*, 1007–1022. https://doi.org/10.1016/j.celrep.2014.09.049.
10. Gupta, R.K., Mepani, R.J., Kleiner, S., Lo, J.C., Khandekar, M.J., Cohen, P., Frontini, A., Bhowmick, D.C., Ye, L., Cinti, S., et al. (2012). Zfp423 expression identifies committed preadipocytes and localizes to adipose endothelial and perivascular cells. Cell Metab. *15*, 230–239. https://doi.org/10.1016/j.cmet.2012.01.010.
11. Tang, W., Zeve, D., Suh, J.M., Bosnakovski, D., Kyba, M., Hammer, R.E., Tallquist, M.D., and Graff, J.M. (2008). White Fat Progenitor Cells Reside in the Adipose Vasculature. Science *322*, 583–586. https://doi.org/10.1126/science.1156232.
12. Rodeheffer, M.S., Birsoy, K., and Friedman, J.M. (2008). Identification of White Adipocyte Progenitor Cells In Vivo. Cell *135*, 240–249. https://doi.org/10.1016/j.cell.2008.09.036.
13. Schwalie, P.C., Dong, H., Zachara, M., Russeil, J., Alpern, D., Akchiche, N., Caprara, C., Sun, W., Schlaudraff, K.U., Soldati, G., et al. (2018). A stromal cell population that inhibits adipogenesis in mammalian fat depots. Nature *559*, 103–108. https://doi.org/10.1038/s41586-018-0226-8.
14. Merrick, D., Sakers, A., Irgebay, Z., Okada, C., Calvert, C., Morley, M.P., Percec, I., and Seale, P. (2019). Identification of a mesenchymal progenitor cell hierarchy in adipose tissue. Science *364*, eaav2501. https://doi.org/10.1126/science.aav2501.
15. Emont, M.P., Jacobs, C., Essene, A.L., Pant, D., Tenen, D., Colleluori, G., Di Vincenzo, A., Jørgensen, A.M., Dashti, H., Stefek, A., et al. (2022). A single-cell atlas of human and mouse white adipose tissue. Nature *603*, 926–933. https://doi.org/10.1038/s41586-022-04518-2.
16. Sárvári, A.K., Van Hauwaert, E.L., Markussen, L.K., Gammelmark, E., Marcher, A.B., Ebbesen, M.F., Nielsen, R., Brewer, J.R., Madsen, J.G. S., and Mandrup, S. (2021). Plasticity of Epididymal Adipose Tissue in Response to Diet-Induced Obesity at Single-Nucleus Resolution. Cell Metab. *33*, 437–453.e5. https://doi.org/10.1016/j.cmet.2020.12.004.
17. Hepler, C., Shan, B., Zhang, Q., Henry, G.H., Shao, M., Vishvanath, L., Ghaben, A.L., Mobley, A.B., Strand, D., Hon, G.C., et al. (2018). Identification of functionally distinct fibro-inflammatory and adipogenic stromal subpopulations in visceral adipose tissue of adult mice. Elife *7*, e39636. https://doi.org/10.7554/eLife.39636.
18. Burl, R.B., Ramseyer, V.D., Rondini, E.A., Pique-Regi, R., Lee, Y.H., and Granneman, J.G. (2018). Deconstructing Adipogenesis Induced by β3-Adrenergic Receptor Activation with Single-Cell Expression Profiling. Cell Metab. *28*, 300–309.e4. https://doi.org/10.1016/j.cmet.2018.05.025.
19. Kahn, C.R., Wang, G., and Lee, K.Y. (2019). Altered adipose tissue and adipocyte function in the pathogenesis of metabolic syndrome. J. Clin. Invest. *129*, 3990–4000. https://doi.org/10.1172/JCI129187.
20. Jeffery, E., Church, C.D., Holtrup, B., Colman, L., and Rodeheffer, M.S. (2015). Rapid depot-specific activation of adipocyte precursor cells at the onset of obesity. Nat. Cell Biol. *17*, 376–385. https://doi.org/10.1038/ncb3122.
21. Wang, Q.A., Tao, C., Gupta, R.K., and Scherer, P.E. (2013). Tracking adipogenesis during white adipose tissue development, expansion and regeneration. Nat. Med. *19*, 1338–1344. https://doi.org/10.1038/nm.3324.
22. Zwick, R.K., Rudolph, M.C., Shook, B.A., Holtrup, B., Roth, E., Lei, V., Van Keymeulen, A., Seewaldt, V., Kwei, S., Wysolmerski, J., et al. (2018). Adipocyte hypertrophy and lipid dynamics underlie mammary gland remodeling after lactation. Nat. Commun. *9*, 3592. https://doi.org/10.1038/s41467-018-05911-0.
23. Zhang, B., Tsai, P.C., Gonzalez-Celeiro, M., Chung, O., Boumard, B., Perdigoto, C.N., Ezhkova, E., and Hsu, Y.C. (2016). Hair follicles' transit-amplifying cells govern concurrent dermal adipocyte production through sonic hedgehog. Genes Dev. *30*, 2325–2338. https://doi.org/10.1101/gad.285429.116.
24. Rivera-Gonzalez, G.C., Shook, B.A., Andrae, J., Holtrup, B., Bollag, K., Betsholtz, C., Rodeheffer, M.S., and Horsley, V. (2016). Skin Adipocyte Stem Cell Self-Renewal Is Regulated by a PDGFA/AKT-Signaling Axis. Cell Stem Cell *19*, 738–751. https://doi.org/10.1016/j.stem.2016.09.002.
25. Shan, B., Barker, C.S., Shao, M., Zhang, Q., Gupta, R.K., and Wu, Y. (2022). Multilayered omics reveal sex- and depot-dependent adipose progenitor cell heterogeneity. Cell Metab. *34*, 783–799.e7. https://doi.org/10.1016/j.cmet.2022.03.012.
26. Biddy, B.A., Kong, W., Kamimoto, K., Guo, C., Waye, S.E., Sun, T., and Morris, S.A. (2018). Single-cell mapping of lineage and identity in direct reprogramming. Nature *564*, 219–224. https://doi.org/10.1038/s41586-018-0744-4.
27. Kong, W., Biddy, B.A., Kamimoto, K., Amrute, J.M., Butka, E.G., and Morris, S.A. (2020). CellTagging: combinatorial indexing to simultaneously map lineage and identity at single-cell resolution. Nat. Protoc. *15*, 750–772. https://doi.org/10.1038/s41596-019-0247-2.
28. Guo, C., Kong, W., Kamimoto, K., Rivera-Gonzalez, G.C., Yang, X., Kirita, Y., and Morris, S.A. (2019). CellTag Indexing: Genetic barcode-based sample multiplexing for single-cell genomics. Genome Biol. *20*, 90. https://doi.org/10.1186/s13059-019-1699-y.
29. Jindal, K., Adil, M.T., Yamaguchi, N., Yang, X., Wang, H.C., Kamimoto, K., Rivera-Gonzalez, G.C., and Morris, S.A. (2024). Single-cell lineage capture across genomic modalities with CellTag-multi reveals fate-specific gene regulatory changes. Nat. Biotechnol. *42*, 946–959. https://doi.org/10.1038/s41587-023-01931-4.

30. Berry, R., and Rodeheffer, M.S. (2013). Characterization of the adipocyte cellular lineage in vivo. Nat. Cell Biol. *15*, 302–308. https://doi.org/10.1038/ncb2696.

31. Kong, W., Fu, Y.C., Holloway, E.M., Garipler, G., Yang, X., Mazzoni, E.O., and Morris, S.A. (2022). Capybara: A computational tool to measure cell identity and fate transitions. Cell Stem Cell *29*, 635–649.e11. https://doi.org/10.1016/j.stem.2022.03.001.

32. Buechler, M.B., Pradhan, R.N., Krishnamurty, A.T., Cox, C., Calviello, A.K., Wang, A.W., Yang, Y.A., Tam, L., Caothien, R., Roose-Girma, M., et al. (2021). Cross-tissue organization of the fibroblast lineage. Nature *593*, 575–579. https://doi.org/10.1038/s41586-021-03549-5.

33. Jacob, T., Annusver, K., Czarnewski, P., Dalessandri, T., Kalk, C., Levra Levron, C., Campamà Sanz, N., Kastriti, M.E., Mikkola, M.L., Rendl, M., et al. (2023). Molecular and spatial landmarks of early mouse skin development. Dev. Cell *58*, 2140–2162.e5. https://doi.org/10.1016/j.devcel.2023.07.015.

34. Phan, Q.M., Fine, G.M., Salz, L., Herrera, G.G., Wildman, B., Driskell, I.M., and Driskell, R.R. (2020). Lef1 expression in fibroblasts maintains developmental potential in adult skin to regenerate wounds. eLife *9*, e60066. https://doi.org/10.7554/eLife.60066.

35. Schep, A.N., Wu, B., Buenrostro, J.D., and Greenleaf, W.J. (2017). ChromVAR: Inferring transcription-factor-associated accessibility from single-cell epigenomic data. Nat. Methods *14*, 975–978. https://doi.org/10.1038/nmeth.4401.

36. Gulyaeva, O., Nguyen, H., Sambeat, A., Heydari, K., and Sul, H.S. (2018). Sox9-Meis1 Inactivation Is Required for Adipogenesis, Advancing Pref-1+ to PDGFRα+ Cells. Cell Rep. *25*, 1002–1017.e4. https://doi.org/10.1016/j.celrep.2018.09.086.

37. Cattaneo, P., Mukherjee, D., Spinozzi, S., Zhang, L., Larcher, V., Stallcup, W.B., Kataoka, H., Chen, J., Dimmeler, S., Evans, S.M., et al. (2020). Parallel Lineage-Tracing Studies Establish Fibroblasts as the Prevailing In Vivo Adipocyte Progenitor. Cell Rep. *30*, 571–582.e2. https://doi.org/10.1016/j.celrep.2019.12.046.

38. Stefkovich, M., Traynor, S., Cheng, L., Merrick, D., and Seale, P. (2021). Dpp4+ interstitial progenitor cells contribute to basal and high fat diet-induced adipogenesis. Mol. Metab. *54*, 101357. https://doi.org/10.1016/j.molmet.2021.101357.

39. Moitra, J., Mason, M.M., Olive, M., Krylov, D., Gavrilova, O., Marcus-Samuels, B., Feigenbaum, L., Lee, E., Aoyama, T., Eckhaus, M., et al. (1998). Life without white fat: a transgenic mouse. Genes Dev. *12*, 3168–3181. https://doi.org/10.1101/gad.12.20.3168.

40. Shook, B.A., Wasko, R.R., Rivera-Gonzalez, G.C., Salazar-Gatzimas, E., López-Giráldez, F., Dash, B.C., Muñoz-Rojas, A.R., Aultman, K.D., Zwick, R.K., Lei, V., et al. (2018). Myofibroblast proliferation and heterogeneity are supported by macrophages during skin repair. Science *362*, eaar2971. https://doi.org/10.1126/science.aar2971.

41. Sun, C., Sakashita, H., Kim, J., Tang, Z., Upchurch, G.M., Yao, L., Berry, W.L., Griffin, T.M., and Olson, L.E. (2020). Mosaic Mutant Analysis Identifies PDGFRα/PDGFRβ as Negative Regulators of Adipogenesis. Cell Stem Cell *26*, 707–721.e5. https://doi.org/10.1016/j.stem.2020.03.004.

42. Al-Mansoori, L., Al-Jaber, H., Madani, A.Y., Mazloum, N.A., Agouni, A., Ramanjaneya, M., Abou-Samra, A.B., and Elrayess, M.A. (2020). Suppression of GATA-3 increases adipogenesis, reduces inflammation and improves insulin sensitivity in 3T3L-1 preadipocytes. Cell. Signal. *75*, 109735. https://doi.org/10.1016/j.cellsig.2020.109735.

43. Xu, H., Sethi, J.K., and Hotamisligil, G.S. (1999). Transmembrane tumor necrosis factor (TNF)-α inhibits adipocyte differentiation by selectively activating TNF receptor 1. J. Biol. Chem. *274*, 26287–26295. https://doi.org/10.1074/jbc.274.37.26287.

44. Huang, H., Song, T.-J., Li, X., Hu, L., He, Q., Liu, M., Lane, M.D., and Tang, Q.-Q. (2009). BMP signaling pathway is required for commitment of C3H10T1/2 pluripotent stem cells to the adipocyte lineage. Proc. Natl. Acad. Sci. USA *106*, 12670–12675. https://doi.org/10.1073/pnas.0906266106.

45. Bowers, R.R., Kim, J.W., Otto, T.C., and Lane, M.D. (2006). Stable stem cell commitment to the adipocyte lineage by inhibition of DNA methylation: Role of the BMP-4 gene. Proc. Natl. Acad. Sci. USA *103*, 13022–13027. https://doi.org/10.1073/pnas.0605789103.

46. Shao, M., Hepler, C., Vishvanath, L., MacPherson, K.A., Busbuso, N.C., and Gupta, R.K. (2017). Fetal development of subcutaneous white adipose tissue is dependent on Zfp423. Mol. Metab. *6*, 111–124. https://doi.org/10.1016/j.molmet.2016.11.009.

47. He, T., Wang, S., Li, S., Shen, H., Hou, L., Liu, Y., Wei, Y., Xie, F., Zhang, Z., Zhao, Z., et al. (2023). Suppression of preadipocyte determination by SOX4 limits white adipocyte hyperplasia in obesity. iScience *26*, 106289. https://doi.org/10.1016/j.isci.2023.106289.

48. Kamimoto, K., Stringa, B., Hoffmann, C.M., Jindal, K., Solnica-Krezel, L., and Morris, S.A. (2023). Dissecting cell identity via network inference and in silico gene perturbation. Nature *614*, 742–751. https://doi.org/10.1038/s41586-022-05688-9.

49. Park, K.W., Waki, H., Villanueva, C.J., Monticelli, L.A., Hong, C., Kang, S., MacDougald, O.A., Goldrath, A.W., and Tontonoz, P. (2008). Inhibitor of DNA binding 2 is a small molecule-inducible modulator of peroxisome proliferator-activated receptor-γ expression and adipocyte differentiation. Mol. Endocrinol. *22*, 2038–2048. https://doi.org/10.1210/me.2007-0454.

50. Qiu, X., Mao, Q., Tang, Y., Wang, L., Chawla, R., Pliner, H.A., and Trapnell, C. (2017). Reversed graph embedding resolves complex single-cell trajectories. Nat. Methods *14*, 979–982. https://doi.org/10.1038/nmeth.4402.

51. Choi, W.I., Yoon, J.H., Choi, S.H., Jeon, B.N., Kim, H., and Hur, M.W. (2021). Proto-oncoprotein Zbtb7c and SIRT1 repression: implications in high-fat diet-induced and age-dependent obesity. Exp. Mol. Med. *53*, 917–932. https://doi.org/10.1038/s12276-021-00628-5.

52. Chao, L.C., Bensinger, S.J., Villanueva, C.J., Wroblewski, K., and Tontonoz, P. (2008). Inhibition of adipocyte differentiation by Nur77, Nurr1, and Nor1. Mol. Endocrinol. *22*, 2596–2608. https://doi.org/10.1210/me.2008-0161.

53. Abdesselem, H., Madani, A., Hani, A., Al-Noubi, M., Goswami, N., Ben Hamidane, H., Billing, A.M., Pasquier, J., Bonkowski, M.S., Halabi, N., et al. (2016). SIRT1 limits adipocyte hyperplasia through c-Myc inhibition. J. Biol. Chem. *291*, 2119–2135. https://doi.org/10.1074/jbc.M115.675645.

54. Eguchi, J., Yan, Q.W., Schones, D.E., Kamal, M., Hsu, C.H., Zhang, M.Q., Crawford, G.E., and Rosen, E.D. (2008). Interferon Regulatory Factors Are Transcriptional Regulators of Adipogenesis. Cell Metab. *7*, 86–94. https://doi.org/10.1016/j.cmet.2007.11.002.

55. Jimenez, M.A., Åkerblad, P., Sigvardsson, M., and Rosen, E.D. (2007). Critical Role for Ebf1 and Ebf2 in the Adipogenic Transcriptional Cascade. Mol. Cell. Biol. *27*, 743–757. https://doi.org/10.1128/MCB.01557-06.

56. Björk, C., Subramanian, N., Liu, J., Acosta, J.R., Tavira, B., Eriksson, A.B., Arner, P., and Laurencikiene, J. (2021). An RNAi Screening of Clinically Relevant Transcription Factors Regulating Human Adipogenesis and Adipocyte Metabolism. Preprint at Endocrinology *162*, bqab096. https://doi.org/10.1210/endocr/bqab096.

57. Wang, Y., and Sul, H.S. (2009). Pref-1 Regulates Mesenchymal Cell Commitment and Differentiation through Sox9. Cell Metab. *9*, 287–302. https://doi.org/10.1016/j.cmet.2009.01.013.

58. Fajas, L. (2003). Adipogenesis: A Cross-Talk between Cell Proliferation and Cell Differentiation. Ann. Med. *35*, 79–85. https://doi.org/10.1080/07853890310009999.

59. Jeffery, E., Wing, A., Holtrup, B., Sebo, Z., Kaplan, J.L., Saavedra-Peña, R., Church, C.D., Colman, L., Berry, R., and Rodeheffer, M.S. (2016). The Adipose Tissue Microenvironment Regulates Depot-Specific Adipogenesis in Obesity. Cell Metab. *24*, 142–150. https://doi.org/10.1016/j.cmet.2016.05.012.

60. Nahmgoong, H., Jeon, Y.G., Park, E.S., Choi, Y.H., Han, S.M., Park, J., Ji, Y., Sohn, J.H., Han, J.S., Kim, Y.Y., et al. (2022). Distinct properties of adipose stem cell subpopulations determine fat depot-specific

characteristics. Cell Metab. *34*, 458–472.e6. https://doi.org/10.1016/j.cmet.2021.11.014.

61. Wernstedt Asterholm, I., Tao, C., Morley, T.S., Wang, Q.A., Delgado-Lopez, F., Wang, Z.V., and Scherer, P.E. (2014). Adipocyte inflammation is essential for healthy adipose tissue expansion and remodeling. Cell Metab. *20*, 103–118. https://doi.org/10.1016/j.cmet.2014.05.005.
62. Bouloumié, A., Planat, V., Devedjian, J.C., Valet, P., Saulnier-Blache, J.S., Record, M., and Lafontan, M. (1994). α2-adrenergic stimulation promotes preadipocyte proliferation: Involvement of mitogen-activated protein kinases. J. Biol. Chem. *269*, 30254–30259. https://doi.org/10.1016/s0021-9258(18)43805-7.
63. Guerrero-Juarez, C.F., Dedhia, P.H., Jin, S., Ruiz-Vega, R., Ma, D., Liu, Y., Yamaga, K., Shestova, O., Gay, D.L., Yang, Z., et al. (2019). Single-cell analysis reveals fibroblast heterogeneity and myeloid-derived adipocyte progenitors in murine skin wounds. Nat. Commun. *10*, 650. https://doi.org/10.1038/s41467-018-08247-x.
64. Zhang, Z., Shao, M., Hepler, C., Zi, Z., Zhao, S., An, Y.A., Zhu, Y., Ghaben, A.L., Wang, M.Y., Li, N., et al. (2019). Dermal adipose tissue has high plasticity and undergoes reversible dedifferentiation in mice. J. Clin. Invest. *129*, 5327–5342. https://doi.org/10.1172/JCI130239.
65. Thompson, S.M., Phan, Q.M., Winuthayanon, S., Driskell, I.M., and Driskell, R.R. (2022). Parallel Single-Cell Multiomics Analysis of Neonatal Skin Reveals the Transitional Fibroblast States that Restrict Differentiation into Distinct Fates. J. Invest. Dermatol. *142*, 1812–1823.e3. https://doi.org/10.1016/j.jid.2021.11.032.
66. Foster, D.S., Januszyk, M., Yost, K.E., Chinta, M.S., Gulati, G.S., Nguyen, A.T., Burcham, A.R., Salhotra, A., Ransom, R.C., Henn, D., et al. (2021). Integrated spatial multiomics reveals fibroblast fate during tissue repair. Proc. Natl. Acad. Sci. USA *118*, e2110025118. https://doi.org/10.1073/pnas.2110025118/-/DCSupplemental.
67. VanHorn, S., and Morris, S.A. (2021). Next-Generation Lineage Tracing and Fate Mapping to Interrogate Development. Dev. Cell *56*, 7–21. https://doi.org/10.1016/j.devcel.2020.10.021.
68. Yamamoto, R., Morita, Y., Ooehara, J., Hamanaka, S., Onodera, M., Rudolph, K.L., Ema, H., and Nakauchi, H. (2013). XClonal analysis unveils self-renewing lineage-restricted progenitors generated directly from hematopoietic stem cells. Cell *154*, 1112–1126. https://doi.org/10.1016/j.cell.2013.08.007.
69. Naik, S.H., Perié, L., Swart, E., Gerlach, C., Van Rooij, N., De Boer, R.J., and Schumacher, T.N. (2013). Diverse and heritable lineage imprinting of early haematopoietic progenitors. Nature *496*, 229–232. https://doi.org/10.1038/nature12013.
70. Xin, T., Gonzalez, D., Rompolas, P., and Greco, V. (2018). Flexible fate determination ensures robust differentiation in the hair follicle. Nat. Cell Biol. *20*, 1361–1369. https://doi.org/10.1038/s41556-018-0232-y.
71. Leung, V.Y.L., Gao, B., Leung, K.K.H., Melhado, I.G., Wynn, S.L., Au, T.Y.K., Dung, N.W.F., Lau, J.Y.B., Mak, A.C.Y., Chan, D., et al. (2011). SOX9 governs differentiation stage-specific gene expression in growth plate chondrocytes via direct concomitant transactivation and repression. PLoS Genet. *7*, e1002356. https://doi.org/10.1371/journal.pgen.1002356.
72. Kumar, S., Liu, J., Pang, P., Krautzberger, A.M., Reginensi, A., Akiyama, H., Schedl, A., Humphreys, B.D., and McMahon, A.P. (2015). Sox9 Activation Highlights a Cellular Pathway of Renal Repair in the Acutely Injured Mammalian Kidney. Cell Rep. *12*, 1325–1338. https://doi.org/10.1016/j.celrep.2015.07.034.
73. Burclaff, J., Bliton, R.J., Breau, K.A., Cotton, M.J., Hinesley, C.M., Ok, M.T., Sweet, C.W., Zheng, A., Bankaitis, E.D., Ariel, P., et al. (2022). SOX9 elongates cell cycle phases and biases fate decisions in human intestinal stem cells. Preprint at bioRxiv. https://doi.org/10.1101/2022.11.03.514885.
74. Tang, Q.-Q., Otto, T.C., and Lane, M.D. (2002). Mitotic Clonal Expansion: A Synchronous Process Required for Adipogenesis. Proc. Natl. Acad. Sci. USA *100*, 44–49. https://doi.org/10.1073/pnas.0137044100.
75. Macotela, Y., Emanuelli, B., Mori, M.A., Gesta, S., Schulz, T.J., Tseng, Y.H., and Kahn, C.R. (2012). Intrinsic differences in adipocyte precursor cells from different white fat depots. Diabetes *61*, 1691–1699. https://doi.org/10.2337/db11-1753.
76. Islam, N., and Garza, L.A. (2018). Adipose and Hair Function: An aPPARent Connection. J. Invest. Dermatol. *138*, 480–482. https://doi.org/10.1016/j.jid.2017.10.019.
77. Vishvanath, L., and Gupta, R.K. (2019). Contribution of adipogenesis to healthy adipose tissue expansion in obesity. J. Clin. Invest. *129*, 4022–4031. https://doi.org/10.1172/JCI129191.
78. Rigamonti, A., Brennand, K., Lau, F., and Cowan, C.A. (2011). Rapid cellular turnover in adipose tissue. PLoS One *6*, e17637. https://doi.org/10.1371/journal.pone.0017637.
79. Bowling, S., Sritharan, D., Osorio, F.G., Nguyen, M., Cheung, P., Rodriguez-Fraticelli, A., Patel, S., Yuan, W.C., Fujiwara, Y., Li, B.E., et al. (2020). An Engineered CRISPR-Cas9 Mouse Line for Simultaneous Readout of Lineage Histories and Gene Expression Profiles in Single Cells. Cell *181*, 1410–1422.e27. https://doi.org/10.1016/j.cell.2020.04.048.
80. Li, L., Bowling, S., McGeary, S.E., Yu, Q., Lemke, B., Alcedo, K., Jia, Y., Liu, X., Ferreira, M., Klein, A.M., et al. (2023). A mouse model with high clonal barcode diversity for joint lineage, transcriptomic, and epigenomic profiling in single cells. Cell *186*, 5183–5199.e22. https://doi.org/10.1016/j.cell.2023.09.019.
81. Ahn, S., Olive, M., Aggarwal, S., Krylov, D., Ginty, D.D., and Vinson, C. (1998). A dominant-negative inhibitor of CREB reveals that it is a general mediator of stimulus-dependent transcription of c-fos. Mol. Cell. Biol. *18*, 967–977. https://doi.org/10.1128/MCB.18.2.9671.
82. Guo, W., Keckesova, Z., Donaher, J.L., Shibue, T., Tischler, V., Reinhardt, F., Itzkovitz, S., Noske, A., Zürrer-Härdi, U., Bell, G., et al. (2012). Slug and Sox9 cooperatively determine the mammary stem cell state. Cell *148*, 1015–1028. https://doi.org/10.1016/j.cell.2012.02.008.
83. Román-Fernández, Á., Roignot, J., Sandilands, E., Nacke, M., Mansour, M.A., McGarry, L., Shanks, E., Mostov, K.E., and Bryant, D.M. (2018). The phospholipid PI(3,4)P2 is an apical identity determinant. Nat. Commun. *9*, 5041. https://doi.org/10.1038/s41467-018-07464-8.
84. Stewart, S.A., Dykxhoorn, D.M., Palliser, D., Mizuno, H., Yu, E.Y., An, D.S., Sabatini, D.M., Chen, I.S., Hahn, W.C., Sharp, P.A., et al. (2003). Lentivirus-delivered stable gene silencing by RNAi in primary cells. RNA *9*, 493–501. https://doi.org/10.1261/rna.2192803.
85. Satija, R., Farrell, J., Gennert, D., Schier, A.F., and Regev, A. (2015). Spatial reconstruction of single-cell gene expression data. Nat. Biotechnol. *33*, 495–502. https://doi.org/10.1038/nbt.3192.
86. Butler, A., Hoffman, P., Smibert, P., Papalexi, E., and Satija, R. (2018). Integrating single-cell transcriptomic data across different conditions, technologies, and species. Nat. Biotechnol. *36*, 411–420. https://doi.org/10.1038/nbt.4096.
87. Stuart, T., Butler, A., Hoffman, P., Hafemeister, C., Papalexi, E., Mauck, W.M., Hao, Y., Stoeckius, M., Smibert, P., and Satija, R. (2019). Comprehensive Integration of Single-Cell Data. Cell *177*, 1888–1902.e21. https://doi.org/10.1016/j.cell.2019.05.031.
88. Kamimoto, K., Adil, M.T., Jindal, K., Hoffmann, C.M., Kong, W., Yang, X., and Morris, S.A. (2023). Gene regulatory network reconfiguration in direct lineage reprogramming. Stem Cell Rep. *18*, 97–112. https://doi.org/10.1016/j.stemcr.2022.11.010.
89. Lu, R., Neff, N.F., Quake, S.R., and Weissman, I.L. (2011). Tracking single hematopoietic stem cells in vivo using high-throughput sequencing in conjunction with viral genetic barcoding. Nat. Biotechnol. *29*, 928–933. https://doi.org/10.1038/nbt.1977.
90. Tang, M., Kaymaz, Y., Logeman, B.L., Eichhorn, S., Liang, Z.S., Dulac, C., and Sackton, T.B. (2021). Evaluating single-cell cluster stability using the Jaccard similarity index. Bioinformatics *37*, 2212–2214. https://doi.org/10.1093/bioinformatics/btaa956.
91. Iglewicz, B., and Hoaglin, D.C. (1993) How to Detect and Handle Outliers (American Society for Quality Control). https://asq.org/quality-press/display-item?item=E0801.

STAR★METHODS

KEY RESOURCES TABLE

REAGENT or RESOURCE	SOURCE	IDENTIFIER
Antibodies		
CD31-PE-Cy7	BD Biosciences	Cat# 561410 ; RRID: AB_10612003
CD45 APC-PE-Cy7	BD Biosciences	Cat# 561868; RRID: AB_10893599
CD29 PE/Dazzle 594	BioLegend	Cat# 102232; RRID: AB_2716170
CD34 PE	BioLegend	Cat# 119301; RRID: AB_345279
DPP4 (CD26) APC	BioLegend	Cat# 137807; RRID: AB_10663403
CD9 BV421	BD Biosciences	Cat# 564235; RRID: AB_2738689
F3	R&D	Cat# AF3178; RRID: AB_2278143
Perilipin A	Abcam	Cat# ab3526; RRID: AB_2167274
tdTomato	LSBio	LS-C3406
Bacterial and virus strains		
CellTag A Lentivirus	Addgene	24591
sh-Sox9 Lentivirus	Addgene	40646
Puro shRNA scramble Lentivirus	Addgene	162011
pCMV-dR8.2 (CellTag Lentivirus packaging)	Addgene	8455
pCMV-VSV-G (CellTag Lentivirus packaging)	Addgene	8454
psPAX2 (shRNA Lentivirus packaging)	Addgene	12260
pMD2.G (shRNA Lentivirus packaging)	Addgene	12259
Stellar Competent Cells	Takara Bio	636763
Chemicals, peptides, and recombinant proteins		
Feta Bovine Serum	GIBCO	10082147
2-Mercaptoethanol	GIBCO	21985023
Antibiotic-Antimycotic	GIBCO	15240062
Collagen I	Thermo Fisher	A1048201
Isobutylmethylxanthine	Sigma	I7018
Dexamethasone	Sigma	D4902
Insulin	Sigma	1882
Prolong Gold anti-fade	Thermo Fisher	P36934
Collagenase 1A	Worthington	LS004196
Live/Dead Fixable Violet	Thermo Scientific	L23105
Critical commercial assays		
Live/Dead Fixable Violet	Thermo Scientific	L23105
Click-iT EdU Flow Cytometry Assay Kit	Invitrogen	C10419
AnnexinV detection	ThermoFisher	A13201
Chromium Single Cell 3′, v3.1 Library & Gel Bead Kit	10× Genomics	PN-1000268
Chromium Single Cell G Chip kit	10× Genomics	PN-1000127
Dual Index Kit TT Set A	10× Genomics	PN-1000215
Deposited data		
Raw Data: GSE241627	This paper	https://www.ncbi.nlm.nih.gov/geo/query/acc.cgi?acc=GSE241627
Processed Seurat Objects	This paper	https://tinyurl.com/5et2bh5n
Experimental models: Cell lines		
293T-17	ATCC	CRL-11268

(*Continued on next page*)

Continued

REAGENT or RESOURCE	SOURCE	IDENTIFIER
Experimental models: Organisms/strains		
C57BL/6J	Jackson Laboratories	000664
Rosa/nTnG	Jackson Laboratories	023035
Oligonucleotides/probes		
5'AATGATACGGCGACCACCGAGAT CTACACTCTTTCCCTACACGACGCTC3'	IDT	P5/R1-par
5'CAAGCAGAAGACGGCATACGAGA TNNNNNNNNGTGACTGGAGTTCAGA CGTGTGCTCTTCCGATCTACAGgta ctggagccgaga3'	IDT	P7/SI-R2_2
Akr1c18	Thermo Fisher	Mm00506289_m1
Smpd3	Thermo Fisher	Mm00491359_m1
Gap43	Thermo Fisher	Mm00500404_m1
Dpp4	Thermo Fisher	Mm00494538_m1
Cd9	Thermo Fisher	Mm00514275_g1
Igfbp7	Thermo Fisher	Mm03807886_m1
Mfap4	Thermo Fisher	Mm00840681_m1
Igf1	Thermo Fisher	Mm00439560_m1
Eln	Thermo Fisher	Mm00514670_m1
Lox	Thermo Fisher	Mm00495386_m1
Smoc2	Thermo Fisher	Mm00491553_m1
Plin1	Thermo Fisher	Mm00558672_m1
Adipoq	Thermo Fisher	Mm00456425_m1
Pparg	Thermo Fisher	Mm00440940_m1
Sox9	Thermo Fisher	Mm00448840_m1
Recombinant DNA		
Cebpa-DN	Ahn et al.[81]	Addgene 33352
CellTag-V1	Biddy et al.[26]	Addgene 115643
CellTag-V2	Biddy et al.[26]	Addgene 115644
CellTag A	Guo et al.[28]	Addgene 124591
sh-Sox9	Guo et al.[82]	Addgene 40646
Puro shRNA scramble	Roman-Fernandez et al.[83]	Addgene 162011
pCMV-dR8.2 (CellTag Lentivirus packaging)	Stewart et al.[84]	Addgene 8455
pCMV-VSV-G (CellTag Lentivirus packaging)	Stewart et al.[84]	Addgene 8454
psPAX2 (shRNA Lentivirus packaging)		Addgene 12260
pMD2.G (shRNA Lentivirus packaging)		Addgene 12259
Software and algorithms		
FlowJo	FLOWJO	https://www.flowjo.com/
Fiji: An Open-Source Platform for Biological-Image Analysis	NIH	https://imagej.net/software/fiji/
Seurat v4.3.0	Satija et al.[85]; Butler et al.[86]; Stuart et al.[87]	https://satijalab.org/seurat/articles/get_started.html
R v4.2.2	R Core Team, 2021	N/A
Cell Ranger v5.0.1	10× Genomics	https://support.10xgenomics.com/single-cell-gene-expression/software/downloads/latest
RStudio	RStudio Team, 2020	https://www.rstudio.com/

(*Continued on next page*)

Continued

REAGENT or RESOURCE	SOURCE	IDENTIFIER
Capybara v0.0.0.9	Kong et al.[31]	https://github.com/morris-lab/Capybara
CellOracle v0.16.0	Kamimoto et al.[48,88]	https://github.com/morris-lab/CellOracle
Code for processing and analysis	This paper	https://doi.org/10.5281/zenodo.15831916.

EXPERIMENTAL MODEL AND STUDY PARTICIPANT DETAILS

Mice

All experiments conducted on mice were performed following the guidelines issued by Washington University in St. Louis or George Washington University's Institutional Animal Care and Use Committee (IACUC) Protocol ID: 21-0317 (WUSTL) and A2023-086 (GWU). C57BL/6J (Strain #:000664), ROSAnTnG (Strain #023035), RosamTmG (Strain #007676), PdgfraCreER (Strain 032770) and *Sox9* floxed (Strain #013106) mice were purchased from Jackson Laboratories and used at least 1 week after arrival. Mice were housed in a 12:12 light-dark cycle with a temperature range between 20-26°C. Chow and water were provided ad libitum. Control and experimental groups were assigned randomly, and male and female mice were used. All mice were subject to visual inspection of the skin to visually evaluate the stage of the hair follicle cycle before experimentation. The number of mice used for each experiment is detailed in the figure legends.

METHOD DETAILS

Adipocyte Precursor Cell Culture

FACS-isolated adipocyte precursors were cultured as described previously from P21 male and female C57BL/6J mice.[24] Briefly, cells sorted via FACS were plated on collagen-coated plates (Collagen I, Cat# A1048201, Thermo Fisher) in DMEM supplemented with 10% fetal bovine serum (FBS), 1X 2-Mercaptoethanol (GIBCO, #21985023) and 1X Antibiotic-Antimycotic (GIBCO, #15240062).

Adipocyte Precursor differentiation

To compare adipogenic differentiation potential among different adipocyte precursor populations, cells were plated at near 100% confluency. After 24 hours, cells were switched to DMEM supplemented with 0.5% FBS for an additional 48 hours, following the procedure described by Merrick et al. After this starvation step, cells were treated with insulin (Sigma, I1882, 2 μg/ml) every 48 hours until harvested for insulin-only differentiation. For MDI-induced differentiation, cells were first treated with 0.5 μM isobutylmethylxanthine (Sigma, I7018), 1 μM dexamethasone (Sigma, D4902), and insulin (2 μg/ml) for 48 hours post-starvation, then switched to insulin-only media for the remainder of the experiment. Prior to RNA extraction, cells were stained with Bodipy (1:1,000; Thermo Fisher, D-3922) and imaged using a Nikon Eclipse Ts2 inverted microscope. To evaluate the impact of Sox9 perturbation on adipogenesis, a similar differentiation procedure was followed, except that cells were initially plated at 50–60% confluency and cultured until they reached full confluency before proceeding with differentiation.

Adipocyte Precursor Cell Transplants

Adipocyte precursor cell populations were isolated via FACS from three-week-old mTmG male and female mice. Approximately 50,000 cells were resuspended in PBS, mixed at a 1:1 ratio with Matrigel, and injected intradermally into the dorsal skin of P21 C57BL/6 recipient mice. Skin from recipient mice was harvested and embedded in optimal cutting temperature (OCT) compound after hair follicles entered full anagen (approximately P31–P37). To determine the *in vivo* differentiation potential of each transplanted cell type, tdTomato-positive (tdTomato+) cells colocalizing with LipidTOX staining were quantified and reported as a percentage of the total tdTomato+ cells detected in the tissue. Differentiation efficiency across cell types was analyzed using a linear mixed-effects model (LMM), considering cell type as a fixed effect and biological replicates as random effects to account for hierarchical experimental structure.

In Vivo Adipocyte Differentiation Potential

To evaluate how *Sox9* deletion affects the in vivo adipogenic potential of adipocyte precursor cells, we crossed PdgfraCreER mice with mTmG reporter and *Sox9*-floxed mice, generating *Pdgfra*CreER; mTmG; *Sox9*$^{flox/flox}$ mice. At P18, these mice received intraperitoneal injections of tamoxifen (50 mg/kg). Skin was harvested at the peak of the anagen phase of hair follicle cycling (approximately P31–P37) and embedded in OCT compound. Skin sections were immunostained for GFP and Perilipin A to quantify the density of newly generated adipocytes per unit length of epidermal surface.

Proliferation and Annexin staining

FACS-isolated cells from male and female C57BL/6J mice at P21 were cultured as previously described.[24] To assess proliferation, cultured cells were incubated with 10 μM EdU (Thermo Fisher Scientific, Cat# C10634) for 24 hours before harvesting. Cells were

subsequently processed according to the manufacturer's instructions for EdU detection. For apoptosis assays, cells were stained with Annexin V conjugate (Thermo Fisher Scientific, Cat# A13199) in 1X Annexin V binding buffer (Thermo Fisher Scientific, Cat# V13246) for 15 minutes at room temperature, followed by washing according to the manufacturer's guidelines.

Immunofluorescence and Tissue Staining

Skin samples from C57BL/6J mice were embedded in OCT compound (Tissue-Tek, Cat# 4583) and rapidly frozen on dry ice. OCT-embedded tissue blocks were sectioned at 14 μm using a cryostat. Tissue sections were fixed in 4% formaldehyde for 10 min and then immunostained as described previously.[24] Primary antibodies used were Perilipin A (ab3526, 1:1000, Abcam) and tdTomato (LSBio, LS-C3406, goat, 1:100). Following primary antibody incubation, sections were stained with DAPI solution (300 nM) for 5 min and then washed. Slides were mounted using Prolong Gold Antifade reagent (Thermo Fisher Scientific, Cat# P36934). Images were acquired with a Zeiss AxioImager Z2 microscope and analyzed using Fiji (NIH) and Adobe Photoshop software.

RNA Extraction and Real-Time PCR

Total RNA extraction and purification were performed using the RNeasy Mini Kit (QIAGEN, Cat# 74104) or RNeasy Micro Kit (QIAGEN, Cat# 74004), according to the manufacturer's instructions. RNA was reverse transcribed into cDNA using the Maxima First Strand cDNA Synthesis Kit (Thermo Fisher Scientific, Cat# K1672). Real-time quantitative PCR was carried out on a StepOne Plus qPCR system using TaqMan™ Gene Expression Master Mix (Thermo Fisher Scientific, Cat# 4371135) with gene-specific TaqMan™ probes in a 20 μl reaction volume, following the manufacturer's recommended protocol. The following TaqMan™ probes were used: *Akr1c18* (Mm00506289_m1), *Smpd3* (Mm00491359_m1), *Gap43* (Mm00500404_m1), *Dpp4* (Mm00494538_m1), *Cd9* (Mm00514275_g1), *Igfbp7* (Mm03807886_m1), *Mfap4* (Mm00840681_m1), *Igf1* (Mm00439560_m1), *Eln* (Mm00514670_m1), *Lox* (Mm00495386_m1), *Smoc2* (Mm00491553_m1), *Plin1* (Mm00558672_m1), *Adipoq* (Mm00456425_m1), *Pparg* (Mm00440940_m1), *Sox9* (Mm00448840_m1).

FACS and Analysis

FACS analysis of adipocyte precursors was conducted as previously described.[24] Briefly, dorsal skin from male and female P21 C57BL/6J mice was dissected and enzymatically digested in collagenase buffer containing Hank's Balanced Salt Solution (HBSS), 3% BSA, Collagenase 1A (Worthington, LS004196; 1:100 dilution), 1.2 mM calcium chloride, and 0.8 mM zinc chloride. Digestion was performed at 37°C for 60 minutes in a shaking water bath. Undigested tissue was separated from released cells through sequential filtration using 100 μm and 70 μm mesh filters. Mature adipocytes were separated from the stromal vascular fraction (SVF) via centrifugation at 300 × g for 3 minutes.

To identify adipocyte precursors, the SVF cells were stained in HBSS supplemented with 3% BSA using the following antibodies: CD31-PE-Cy7 (1:500; BD Biosciences, 561410), CD45 APC-PE-Cy7 (1:5000; BD Biosciences, 561868), CD29 PE/Dazzle 594 (1:400; BioLegend, 102232), CD34 PE (1:200; BioLegend, 119301), DPP4 (CD26) APC (1:500; BioLegend, 137807), CD9 BV421 (1:250; BD Biosciences, 564235), and F3 (1:100; R&D, AF3178). For live/dead discrimination, cells were stained with Live/Dead Fixable Violet (1:1000; Thermo Scientific, L23105).

Cell proliferation analysis via EdU incorporation was conducted using the Click-iT EdU Flow Cytometry Assay Kit (Invitrogen, C10419), according to the manufacturer's instructions. For apoptosis detection, cells were stained with fluorescent Annexin V (Thermo Fisher Scientific, A13201) following the manufacturer's protocols. Cell sorting and data acquisition were performed using either a Sony iCyt Synergy BSC or a Beckman Coulter CytoFLEX SRT instrument. Flow cytometry data analysis was conducted using FlowJo software.

CellTag and plasmids

CellTag v1 and v2 lentiviral constructs were generated by introducing an 8-bp variable region into the 3′ UTR of GFP in the pSmal plasmid (Addgene, #24593)[89] using a gBlock gene fragment (Integrated DNA Technologies) and megaprimer insertion (protocol available at https://www.addgene.org/pooled-library/morris-lab-celltag/). The dominant-negative form of Cebpa (Cebpa-DN; Addgene, #33352) was cloned into the CellTag A plasmid (Addgene, #24591). Individual barcode clones from CellTag-multi[29] were selected and verified via Sanger sequencing to generate predefined barcodes. *Sox9* was cloned into the CellTag_F plasmid under control of the SFFV promoter using the barcode sequence: ATAGTATTCTGACAGGTATGAGCCATCT. Sox9-shRNA-treated cells were tagged with CellTag_D (barcode: TAGGTGTGCTATTAGATATGTCACATAG), and control cells were tagged with CellTag_A (barcode: TTCGTAGCCTGTCAGCTATGGTTCATAG). Lentiviral vectors pLKO.1-sh-mSOX9-5 (#40646) and pLKO.1 puro shRNA scramble control (#162011) were obtained from Addgene.

Lentivirus production

CellTag lentiviruses were produced by transfecting HEK293T cells with lentiviral pSMAL vector and packing plasmids pCMV-dR8.2 dvpr (Addgene plasmid 8455) and pCMV-VSV-G (Addgene plasmid 8454) using X-tremeGENE 9 (Sigma-Aldrich). ShRNA lentiviruses were produced by transfecting HEK293T cells with pLKO.1 plasmids and packaging plasmids psPAX2 (Addgene, 12260) and pMD2.G (Addgene, 12259). Viruses were collected 48 and 72 h after transfection.

Virus transduction

Viral supernatants containing CellTag, CEBP-DN, *Sox9*-shRNA, or scrambled shRNA were collected from transfected HEK293T cells, stored at 4°C, and used within one week. Immediately before transduction, protamine sulfate (Sigma-Aldrich) was added to a final concentration of 4 μg/mL. Cells were transduced by aspirating culture media and adding the viral mixture combined with complete media for 12-hour incubation periods. For adipocyte precursors transduced with a single virus type (CellTag, CEBP-DN, or shRNA), this transduction process was repeated once (total 24 hours). For cells receiving two different viral types, the procedure was repeated three additional times (total 48 hours). Successful *Sox9* knockdown via shRNA was verified by measuring *Sox9* expression in sampled cells before transplantation into the skin.

Transplantation Assay for virus-treated cells

Adipocyte precursors were isolated via FACS from P21 C57BL/6J male and female mice, treated with the corresponding viruses, and then resuspended in PBS. Cells were mixed 1:1 with Matrigel (Corning, #356231) and injected intradermally into the dorsal skin or directly into the inguinal adipose depot of P21 recipient C57BL/6J mice.

For inguinal depot transplantation, P21 mice were anesthetized using isoflurane (0.5–2%, flow rate 0.4–0.8 L/min). Hair was removed from the dorsal area proximal to the hind legs to visualize the inguinal adipose depot beneath the skin. The area was sterilized with ethanol and Betadine to maintain aseptic conditions. A 2 mm cutaneous incision was then made to expose the inguinal adipose tissue. Approximately 30 μl of the cell-Matrigel mixture was injected directly into the inguinal depot using a Hamilton syringe. The incision was closed with a single skin clip, removed several days later upon healing.

For competitive progenitor/preadipocyte assays using v1/v2 CellTag libraries, each recipient mouse received injections containing a total of 400,000–500,000 cells (50% v2 progenitors, 50% v1 preadipocytes). For non-competitive skin progenitor transplantation into the inguinal depot, 400,000 total cells were injected. For non-competitive *Sox9* overexpression (OE) and knockdown (KD) transplants, 300,000–400,000 progenitors were injected intradermally into the dorsal skin. In competitive *Sox9* assays, 200,000 cells from each experimental condition were injected into the dorsal skin.

At postnatal day 32–35 (P32–35), dorsal skin or inguinal adipose tissues from recipient mice were harvested and analyzed for transplanted GFP-positive cells and host GFP-negative cells. For competitive assays, GFP-positive and GFP-negative cells were isolated without antibody labeling using the previously described FACS protocol, and then mixed in equal proportions for single-cell library preparation. In non-competitive progenitor transplants into the inguinal depot, GFP-positive lineage-negative cells were isolated. For non-competitive *Sox9* OE and KD assays, GFP-positive and GFP-negative adipocyte precursors were identified and isolated by FACS using CD31/CD45, CD34, DPP4, and CD9 markers. For competitive *Sox9* OE assays, GFP-positive and GFP-negative adipocyte precursors were sorted based on the phenotype CD31/45$^{neg/}$CD34^{high} and subsequently mixed in equal numbers for single-cell library preparation.

scRNA-seq and scATAC-seq

Single-cell RNA sequencing (scRNA-seq) libraries were prepared using the Chromium Single Cell 3′ v3.1 Library & Gel Bead Kit (10X Genomics, PN-1000268), the Chromium Single Cell G Chip Kit (10X Genomics, PN-1000127), and the Dual Index Kit TT Set A (10X Genomics, PN-1000215). Cells were isolated via FACS (as described above), counted, and resuspended in RF enzyme mix. Subsequently, cells were loaded onto a Chromium Single Cell B Chip for generation of gel beads-in-emulsion (GEMs). cDNA purification and sequencing library construction were performed following the manufacturer's protocol. Final libraries were sequenced on an Illumina NextSeq 500 instrument.

To simultaneously profile chromatin accessibility and gene expression within adipocyte precursor populations, we performed single-cell multiome sequencing using the Chromium Next GEM Single Cell Multiome ATAC + Gene Expression platform (10X Genomics, PN-1000283). Freshly isolated cells were counted and resuspended in ice-cold 1X PBS containing 0.04% BSA prior to nuclei isolation and library preparation, adhering strictly to the manufacturer's recommended protocol. Nuclei were transposed using the Chromium Next GEM Single Cell Multiome ATAC Kit A (10X Genomics, PN-1000280), loaded onto a Chromium Next GEM Chip J (10X Genomics, PN-1000230), and partitioned into GEMs using the Chromium Controller. Libraries were constructed using the Chromium Next GEM Single Cell Multiome Reagent Kit A (10X Genomics, PN-1000282) and the Library Construction Kit (10X Genomics, PN-1000190). Sequencing was performed on an Illumina NextSeq 500 instrument.

CellTag amplification for scRNA-seq (CellTag-RNA PCR)

CellTag barcodes from single-cell cDNA libraries generated in Sox*9*-OE and Sox*9*-KD assays were amplified via PCR. cDNA obtained from step 2.4 of the 10x Genomics Single Cell Gene Expression library preparation protocol (CG000315) was used. Briefly, 5 μL (minimum 60 ng) of cDNA was combined with 2× Q5 High-Fidelity PCR Master Mix (New England Biolabs) and 500 nM of each primer (P5/R1-par and P7/SI-R2) in a total reaction volume of 50 μL. The PCR cycling conditions were as follows: initial denaturation at 98°C for 30 seconds, followed by N cycles of 98°C for 10 seconds, 54°C for 30 seconds, and 72°C for 30 seconds, with a final extension at 72°C for 2 minutes. The cycle number (N) was identical to that used during the sample index PCR of the primary scRNA-seq library.

Following amplification, CellTag amplicon libraries were purified using double-sided bead purification (0.4×-0.64×) and quantified on an Agilent TapeStation using D1000-HS tapes. Amplicon libraries were sequenced alongside scRNA-seq libraries on an Illumina NextSeq 500 instrument.

Primer sequences

P5/R1-par 5'AATGATACGGCGACCACCGAGATCTACACTCTTTCCCTACACGACGCTC3' and P7/SI-R2_2 Indexed primer 5'CAAGCAGAAGACGGCATACGAGATNNNNNNNNGTGACTGGAGTTCAGACGTGTGCTCTTCCGATCTACAGgtactggagccgaga3'

Basic data alignment and processing

After demultiplexing, sequencing data were aligned using CellRanger software versions 5.0.1, 6.0.2, 6.1.2, or 7.0.1 (10X Genomics; https://support.10xgenomics.com/single-cell-gene-expression/software/downloads/latest). Alignment was performed against a custom reference genome built upon the mm10 genome, supplemented with sequences for GFP and the dominant-negative form of CEBP-A (DN-CEBPA). Filtered digital gene expression matrices were generated for each sample using CellRanger for downstream analysis, and corresponding BAM files were simultaneously created for CellTag barcode processing.

All single-cell data analyses were conducted using R (version 4.2.2) with Seurat (version 4.3.0). Following the standard Seurat processing pipeline (https://satijalab.org/seurat/articles/pbmc3k_tutorial.html), we filtered out low-quality cells based on two criteria: a high fraction of mitochondrial gene reads (>5%) and low total RNA molecule counts (<500). Cell cycle phase scoring and subsequent regression were performed to minimize cell-cycle-related variability. Uniform Manifold Approximation and Projection (UMAP) was employed for dimensionality reduction, using the top 10 principal components. Louvain clustering was performed with a resolution parameter of 0.75. All other parameters for UMAP embedding and Louvain clustering were set to default values in Seurat.

Data visualizations were generated with the ggplot2 package (version 3.4.2). Unless otherwise stated, statistical tests were performed using the stats package included in R (version 4.2.2).

Integration

Four P32 independent biological replicates were identically prepared and sequenced in pairs at two different times, so pairs of datasets sequenced together were integrated using the Seurat functions *FindIntegrationAnchors()* and *IntegrateData()*. The four datasets were comprised of 5,001, 4,180, 4591, and 5,663 APCs following data processing and filtering. Integrated objects were re-scaled, re-clustered, and re-embedded. Louvain clusters expressing high levels of features identified in Table S2 were removed from both datasets, while clusters expressing high levels of APC markers or GFP were retained. Finally, both datasets were integrated again using the same Seurat integration procedure. The same re-embedding and clustering procedures were re-implemented downstream of integration on the new object.

CellTag index extraction

A standard workflow was utilized in indexing experiments to perform clone calling, with "clones" approximated as cells with a shared CellTag index (https://github.com/morris-lab/newCloneCalling). Here, the bam file was parsed for CellTag reads using the "multi-v1" CellTag version. One unique CellTag per cell was considered an adequate CellTag signature in filtering due to the high library complexity, and cells with greater than 20 unique CellTags were removed. Allowlisting and binarization were performed, but Jaccard and additional downstream clonal analyses were not performed due to the nature of these indexing experiments and lack of biologically informative clonal information.

Published reference cell type classification

Two reference datasets used for Capybara (https://github.com/morris-lab/Capybara) analyses provided publicly available counts and cell type classifications. Cell type annotations and raw counts for 32,194 filtered cells were obtained directly from ArrayExpress (E-MTAB-1192033). These data were used without additional filtering to generate a Capybara reference. Similarly, raw counts and annotations for 120,583 cells from the steady-state mouse fibroblast atlas were downloaded from https://www.fibroxplorer.com/download and used directly as a Capybara reference.

When cell type metadata were not publicly available, we reconstructed cell type annotations by following published parameters described by the original authors. Specifically, raw data were processed according to quality control criteria detailed in the respective publications. Data were subsequently clustered using the Louvain algorithm and embedded with UMAP, both implemented via default parameters in Seurat. As precise cluster assignments were not always explicitly available, our annotations represent best approximations based on marker genes described in the original publications. These approximations enabled generation of accurate Capybara reference datasets.

For the Merrick et al. dataset (GSE128889), raw data comprising lineage-depleted stromal vascular fraction (SVF) from inguinal adipose tissue were processed by filtering cells with $\leq$500 genes detected or $\geq$5% mitochondrial UMIs. Following Louvain clustering, cell types were manually annotated based on expression of previously reported marker genes: interstitial progenitors (high *Dpp4, Wnt2, Bmp7, Pi16*), committed preadipocytes (*high Icam1, Dlk1, Pparg, Fabp4, Cd36*), undefined group 3 (high *Clec11a, Fmo2, F3/Cd142*), undefined group 4 (high *Wnt6, Sfrp5*), undefined group 5 (high *Egfl6, Emb, Dlk1*; low *Icam1*), undefined group 6 (high *Thbs4, Plxdc1*), adipocytes (high *Adipoq, Plin1, Car3*), smooth muscle cells (high *Acta2*, *Myo*-related factors), endothelial cells (high *Pecam1*), and neural crest cells (high *Mpz*). See Cell Typing Supplement.

For the Burl et al. dataset (SRP145475), raw data from untreated (control) lineage-negative inguinal adipocyte stem cells (ASCs) (8,131 cells) were obtained. No additional filtering was performed due to the absence of specified filtering criteria in the original publication. Following Louvain clustering, cells were annotated based on published markers as ASC1 (high *Icam1, Col4a2, Cav1, G0s2*) or ASC2 (high *Pi16, Dpp4*).

For the Phan et al. dataset (GSE153596), raw data encompassing developmental, regenerating, homeostatic, and scarring mouse back skin samples were integrated and clustered. Subsequent cell type classification focused solely on the homeostatic cells isolated at postnatal day 21 (P21) to create a Capybara reference. Cells were manually annotated based on distinctive gene expression signatures: keratinocytes (high *Krt14*), fibroblasts (high *Twist2, Pdgfra, En1*), lymphocyte/blood lineage cells (high *Tyrobp*), and pericytes (high *Rgs5, Acta2*).

Cell type classification by Capybara

We evaluated our datasets for automatic cell type classification with various references according to the published Capybara workflow and the R package Capybara (v0.0.0.9; https://github.com/morris-lab/capybara). We did not perform tissue-level classification; instead, raw counts were used for each dataset to generate a custom reference with classifications constructed as described in each case. Quadratic programming, discrete cell type classification, and multiple identity scoring were performed for downstream analysis. Quadratic programming (QP) scores were generated for each cell in the dataset for each cell type in the reference by parsing the terms of a linear equation that describes a cell's transcriptome as a sum of partial identities of each reference cell type's representative transcriptome.[31]

Differential expression and multiome analysis

Differentially expressed features were identified using the *FindMarkers()* function in Seurat. In all instances, default parameters were used: a 0.25 log fold-change was required between the two groups, a Wilcoxon Rank Sum test was used to identify features, and a minimum fraction of .1 cells expressing the feature in either population was required for testing. Using multiome data, ChromVAR TF Activity deviation scores were computed using the RunChromVAR function in the Signac package for scATAC-seq data analysis and all vertebrate TF motifs from the JASPAR 2020 database. TF activity markers were obtained using the FindAllMarkers function.

Jaccard similarities and modified z score procedure

To calculate Jaccard similarities of Louvain clusters of our P32 data and Capybara classifications of progenitors and committed preadipocytes, we used the *PairWiseJaccardSets()* function of the R package scclusteval (v1.0).[90] Preserving numbers of cells classified as progenitor or committed preadipocyte and sizes of Louvain clusters, we randomized these classifications and calculated pairwise Jaccard distances of randomized data 1,000 times to generate a background distribution of Jaccard values for each pair of cell type classification and Louvain cluster. Because we could not confirm that each of these distributions was normal using a Shapiro Wilk test for normality (data not shown), we calculated a modified z-score for each Jaccard value against its corresponding background distribution to determine outliers in our correlation data.[91] The modified z-score procedure considers the median and median absolute deviation (MAD) in place of the mean and standard deviation, respectively, that are used in a traditional z-score procedure. For a Jaccard value J_i, the modified z-score z_i is calculated against a background distribution D_i as:

$$z_i = \frac{0.6745 * (J_i - median(D_i))}{MAD(D_i)}$$

Outliers are defined as values of z such that $|z| > 3.5$. Further, 0.6745 is used as a constant to correct modified z-scores, as the expectation of the MAD is approximately $0.6745 \cdot \sigma$, or the standard deviation of a normally distributed randomized background.

CellOracle analysis

We evaluated gene regulatory networks and simulated perturbations of all active transcription factors using the published CellOracle workflow and python package (v0.16.0; https://github.com/morris-lab/CellOracle). First, a new embedding was generated of the data using the reverse graph embedding method implemented by Monocle2 (https://cole-trapnell-lab.github.io/monocle-release/docs/). The Monocle2 method described here works well for CellOracle among other dimension reduction methods, as it promotes interpretable predictions by forcing cells into narrow, linear embeddings. The vector-based nature of CellOracle performs best when opposing vectors among a population of cells in an embedding are minimized. Additionally, pseudotime values were generated using the DDRTree algorithm also implemented in the Monocle2 package. Cells were ordered in pseudotime by selecting a state of the embedding with the highest number of progenitor cells to be the root of the embedding and thus cells in this state to be assigned the lowest values of pseudotime.

Using both embedding and pseudotime information generated by Monocle2 coupled with normalized scRNA counts, we performed both systematic knockout and upregulation simulations for each active TF in our dataset. Each knockout simulation is performed by perturbing a single TF at a time, setting expression levels to zero across all cells in the dataset. Similarly, upregulation simulations are performed on one TF at a time, setting expression levels uniformly across all cells artificially to 95% of the maximum observed value of that TF in the scRNA data. Perturbation scores (PS) for both types of simulations are generated, representing the relationship of the predicted effects of the simulation with calculated pseudotime values. A positive PS denotes that CellOracle predicts the simulation will promote differentiation, while a negative PS suggests a predicted block of differentiation when the TF is perturbed. Perturbation scores are generated for each cell type, with the global PS representing the sum of all cell type-specific PSs.

Finally, density plots were generated using a custom script available at https://github.com/morris-lab/adipogenesis-reproducibility-repo. Here, diffusion simulations were performed using Markov chains to visualize shifts in cell density of cells in a selected region of the Monocle2 embedding. First, the left-most region of the embedding was selected as it contains the most cells

in the progenitor state. Diffusion simulations were performed and 1, 6, and 15 steps in the Markov chain were selected to visualize the most complete shifts toward differentiation, when that phenotype was predicted. Hyper parameters were tuned for visualization, and consistent parameters were used for all simulations. Diffusion simulations of selected perturbations are overlaid with density plots of pseudotime shifts with the same cells, parameters, and steps in the Markov chain.

Randomized testing of enrichment of CellTag populations and cell type classifications

To determine Louvain clusters of our P32 data that are enriched for one or both CellTagged populations, we used a custom Python-based script described by Biddy et al.[26] To determine whether cell types are differentially enriched among our CellTagged populations relative to one another or a control, we performed a randomization procedure of pooled cell type classifications for cells in each pair of populations. After pooling, we randomly reassigned cell types to one population or the other, with population sizes preserved. This was performed 10,000 times, generating a null distribution model representing the difference of fractions of each cell type to the population size in each pair of populations. Finally, a two-tailed p-value was calculated, representing the number of the absolute values of these differences that are greater than or equal to the absolute value of the observed difference between the two populations. Bonferroni multiple testing correction was performed to control for dependent alternative hypotheses.

Randomized testing for enrichment and depletion of clone types

We define biased clones as those in which a single cell type constitutes more than 50% of the cells in that clone. Clones with exactly 50% composition of two different cell types are classified as 'split' clones. To assess significant enrichment or depletion of lineage relationships, we performed randomization testing. Clone type classifications (ten in total, across biased and split outcomes) were shuffled across each clone (n = 168 clones of progenitor origin, 59 of preadipocyte origin, each containing 2–4 cells while preserving the clone size distribution). For each randomized dataset, we counted the number of clones biased toward each clone type. This process was repeated 10,000 times to generate a background distribution, against which we calculated a z-score for the observed values. A |z-score| > 1.645 was considered significant.

Bodipy staining quantification

Fluorescence microscopy images were analyzed using ImageJ software. Briefly, each image was opened in ImageJ, and a region of interest (ROI) encompassing the entire image was defined. The parameters 'Area,' 'Mean,' and 'Integrated Density' were measured for each ROI. To account for background fluorescence, three regions lacking fluorescent signal were separately selected and similarly measured within each image. Corrected total cell fluorescence (CTCF) values were calculated using the formula:

$$CTCF = \text{Integrated Density} - (\text{Area of selected ROI} \times \text{Mean fluorescence of background}) \quad \text{(Equation 1)}$$

These CTCF values were subsequently used for downstream statistical analyses and graphical representations.

QUANTIFICATION AND STATISTICAL ANALYSIS

All statistical analyses were conducted using R (version 4.2.2). Differential gene expression analyses from scRNA-seq data were performed using the Wilcoxon rank sum test with Bonferroni correction implemented in Seurat (version 4.3.0). For randomized testing of clonal enrichment and depletion, z-scores were calculated relative to randomized distributions, with significance defined as $|z| > 1.645$. Linear mixed-effects models were used to analyze differentiation efficiencies of transplanted APC populations, with cell type as a fixed effect and biological replicates as random effects. Cell proliferation and apoptosis assays were analyzed using unpaired two-tailed t-tests with Welch's correction for unequal variance. GO enrichment analyses were performed using Fisher's exact tests. ChromVAR TF activity deviation scores were computed using the RunChromVAR function implemented in Signac, with default parameters. No formal statistical methods were used to predetermine sample sizes; however, sample sizes are consistent with previously published studies. Detailed statistical parameters, including specific tests, sample sizes (n), and definitions of n, are provided in the respective figure legends. Data are presented as mean ± standard error of the mean (SEM) unless otherwise indicated, with statistical significance defined as $p < 0.05$, adjusted for multiple comparisons where applicable.

Cell Stem Cell, Volume *32*

Supplemental Information

Comparative single-cell lineage tracing identifies distinct adipocyte precursor dynamics in skin and inguinal fat

Guillermo C. Rivera-Gonzalez, Emily G. Butka, Carolynn E. Gonzalez, Rachel L. Mintz, Sarah S. Kleb, Violet Josephson, Wenjun Kong, Kunal Jindal, Kenji Kamimoto, Brett A. Shook, Matthew S. Rodeheffer, and Samantha A. Morris

Figure S1 (Related to Figure 1)

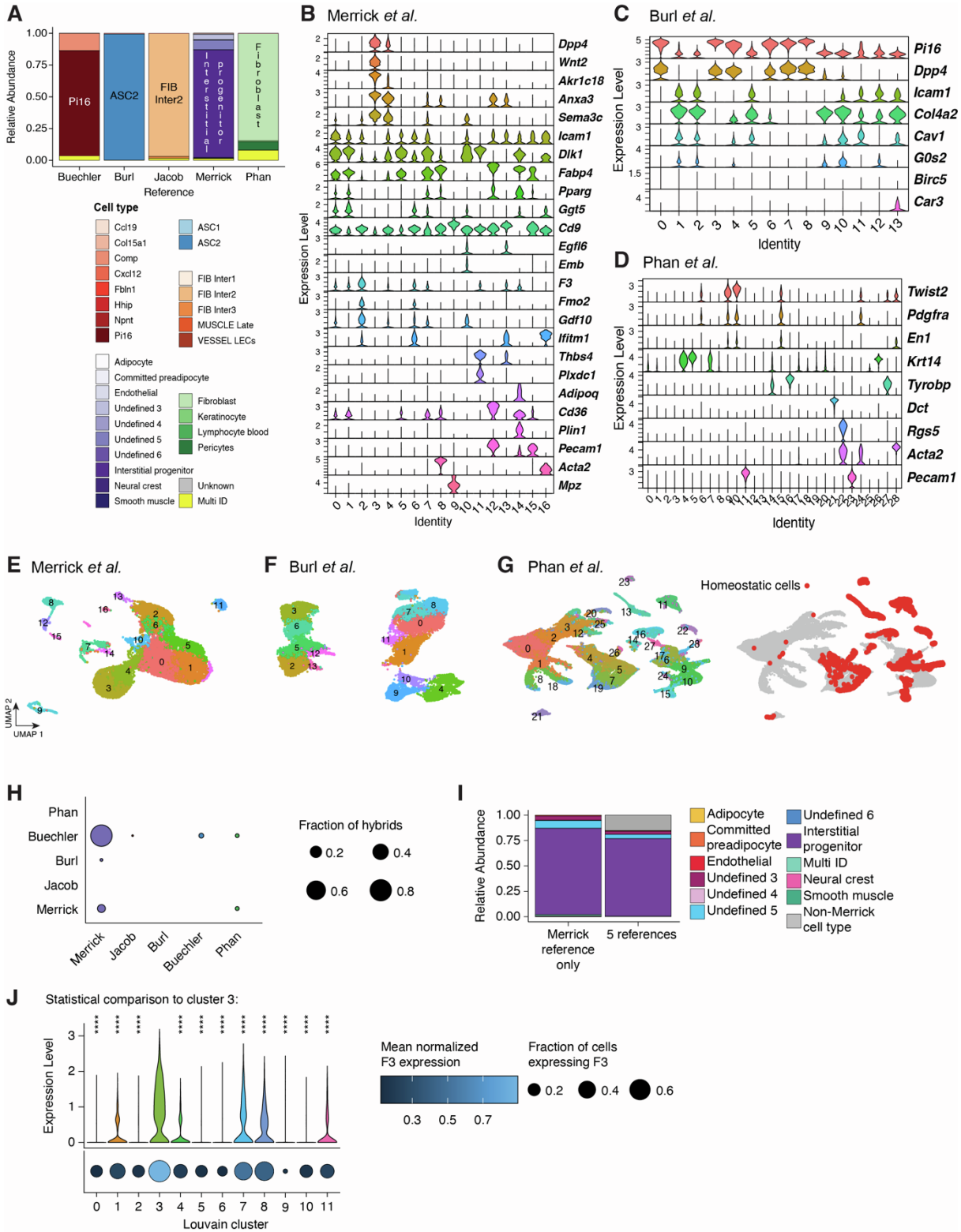

Figure S1. Comparative analysis and integration of reference datasets for classification of skin adipocyte precursor cells. (**A**) Proportions of cell types identified by Capybara classification of postnatal day 21 (P21) skin APCs, based on five publicly available reference datasets.
(B) Manual cluster classification of SVF cells based on reported markers from Merrick et al.
(C) Manual cluster classification of Lin- inguinal WAT ASCs based on reported markers from Burl, et al.
(D) Manual cluster classification of unsorted cells from mouse back skin in Phan, et al.
(E) UMAP embedding of lineage-depleted stromal vascular fraction (SVF) from inguinal adipose tissue (Merrick, D. et al.).
(F) UMAP embedding of Lin- inguinal WAT adipocyte stem cells (ASCs) from Burl, et al.
(G) Left: UMAP embedding of developing, regenerating, homeostatic, and scarring samples of unsorted cells from mouse back skin in Phan, et al. Right: Indication of homeostatic cells from mouse back skin collected at P21 in UMAP embedding from Phan, et al.
(**H**) Composition of hybrid "Multi ID" cells identified by Capybara, showing the contribution from each dataset when the five references were combined into a consolidated reference.
(**I**) Comparison of cell type proportions in P21 APCs classified by Capybara using the Merrick et al. reference alone versus the combined five-dataset reference.
(**J**) Violin plot illustrating *F3* expression across Louvain clusters.

Figure S2 (Related to Figure 2)

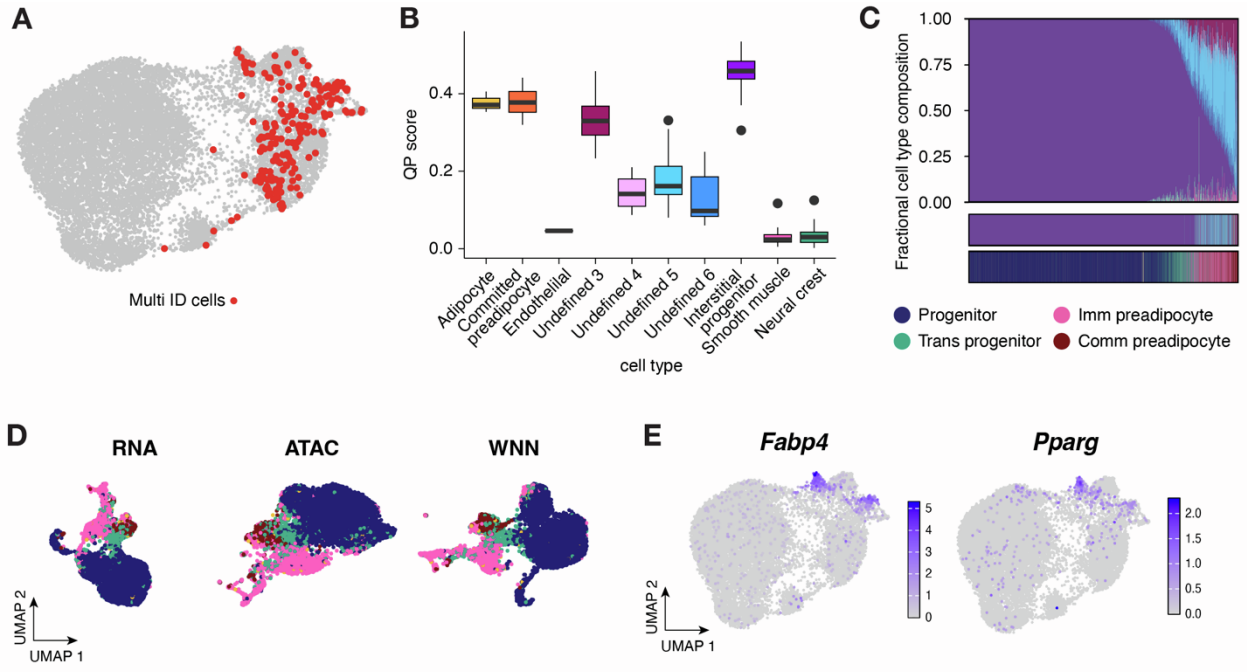

Figure S2. Molecular characterization of adipocyte precursor cell identities in mouse skin.
(**A**) UMAP visualization highlighting "Multi ID" hybrid cells classified by Capybara using the Merrick et al. reference dataset.
(**B**) Transitional cell identities represented by quadratic programming (QP) scores across multiple cell types for cells classified as Multi ID.
(**C**) Normalized QP scores depicting each cell type for individual cells, ranked by decreasing interstitial progenitor identity (top; colors match legend in (B)), Capybara-based cell type classification (middle), and the newly defined skin-specific cell type classification (bottom).
(**D**) Single-cell multiome UMAP embeddings showing RNA, ATAC, and Weighted Nearest Neighbors (WNN) co-embedding of RNA and ATAC data (n = 8,279 cells).
(**E**) Feature plots illustrating expression of adipogenic markers *Fabp4* and *Pparg* within the UMAP embedding.

Figure S3 (Related to Figure 3)

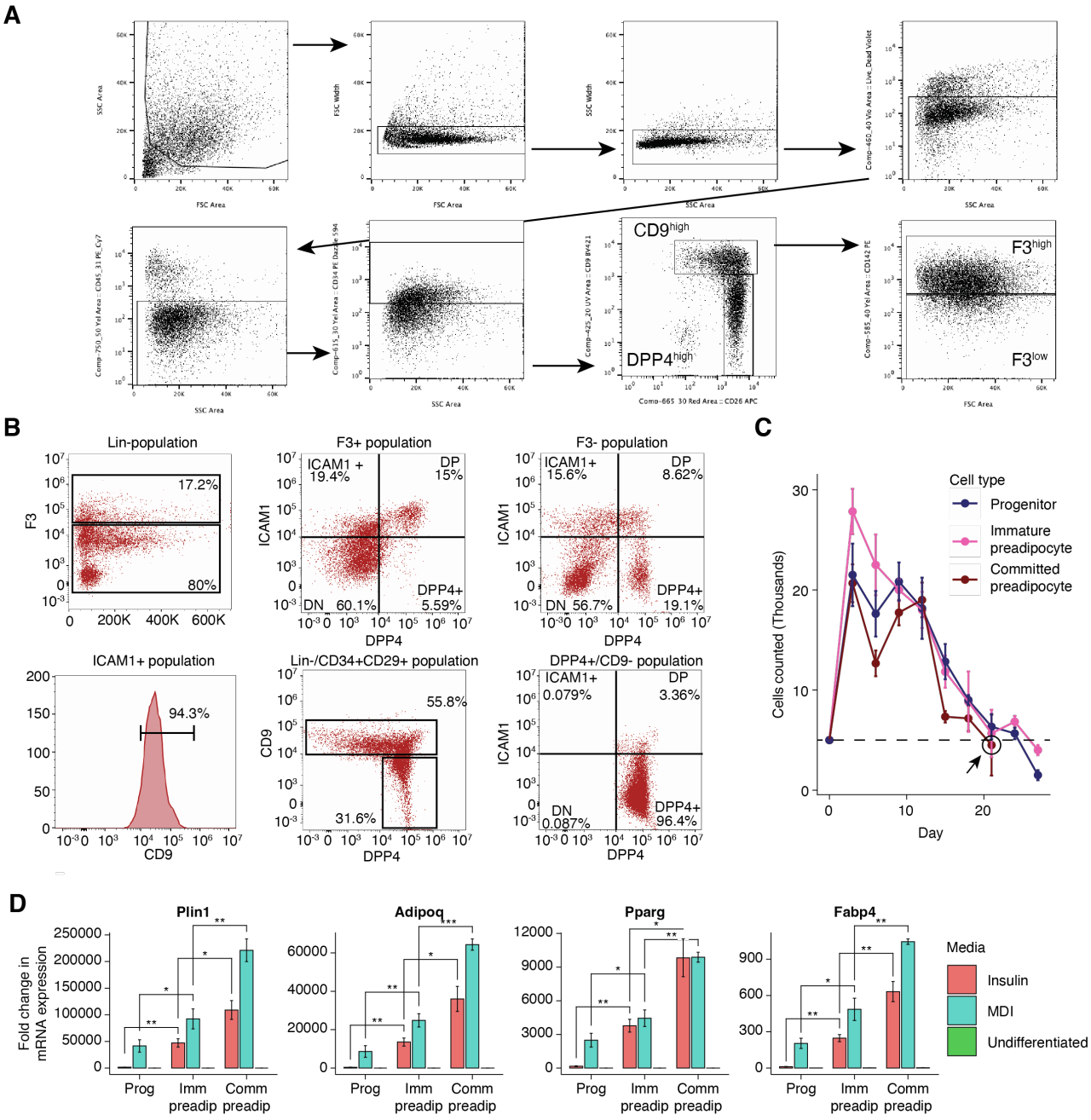

Figure S3. FACS strategy for isolation and establishment of adipogenic potential of progenitors, immature, and committed/undefined group 3 preadipocytes from C57BL/6J P21 mouse skin.

(**A**) FACS gating strategy illustrating sequential cell sorting: after singlet discrimination, live cells were selected, followed by exclusion of CD45+/CD31+ lineage-positive cells. Live, lineage-negative cells were gated for CD34+/CD29+ expression. From these, cells expressing DPP4^{high}/CD9^{low} were isolated as progenitors. CD9^{high} cells were further sorted based on F3

expression: $F3^{high}$ cells identified as immature preadipocytes and $F3^{low}$ cells as committed/group 3 preadipocytes.
(**B**) Detailed FACS profiles for APC populations. Upper left panel: distribution of F3 expression in lineage-negative skin cells. Upper middle panel: ICAM1 and DPP4 expression in putative "group 3" preadipocytes. Upper right panel: identification of adipocyte progenitors and preadipocytes among Lin-/F3- cells by DPP4 and ICAM1 expression. Lower left panel: CD9 expression of preadipocytes within Lin-/F3-/ICAM1+ cells. Lower middle panel: separation of progenitors and preadipocytes from Lin-/CD34+/CD29+ cells by DPP4 and CD9 expression. Lower right panel: ICAM1 expression of progenitors (Lin-/CD34+/CD29+/CD9-/DPP4+ cells).
(**C**) Cell proliferation analysis of APC populations seeded at an initial density of 5,000 cells, counted every 72 hours (n = 3 biological replicates). Dashed line represents the initial seeding density, indicating the "cell renewal" threshold; arrow highlights the loss of self-renewal capacity in committed preadipocytes by day 21.
(**D**) Quantitative PCR (qPCR) analysis measuring expression of adipocyte-specific genes in differentiating APC cultures (related to Figure 3E).

Figure S4 (Related to Figure 4)

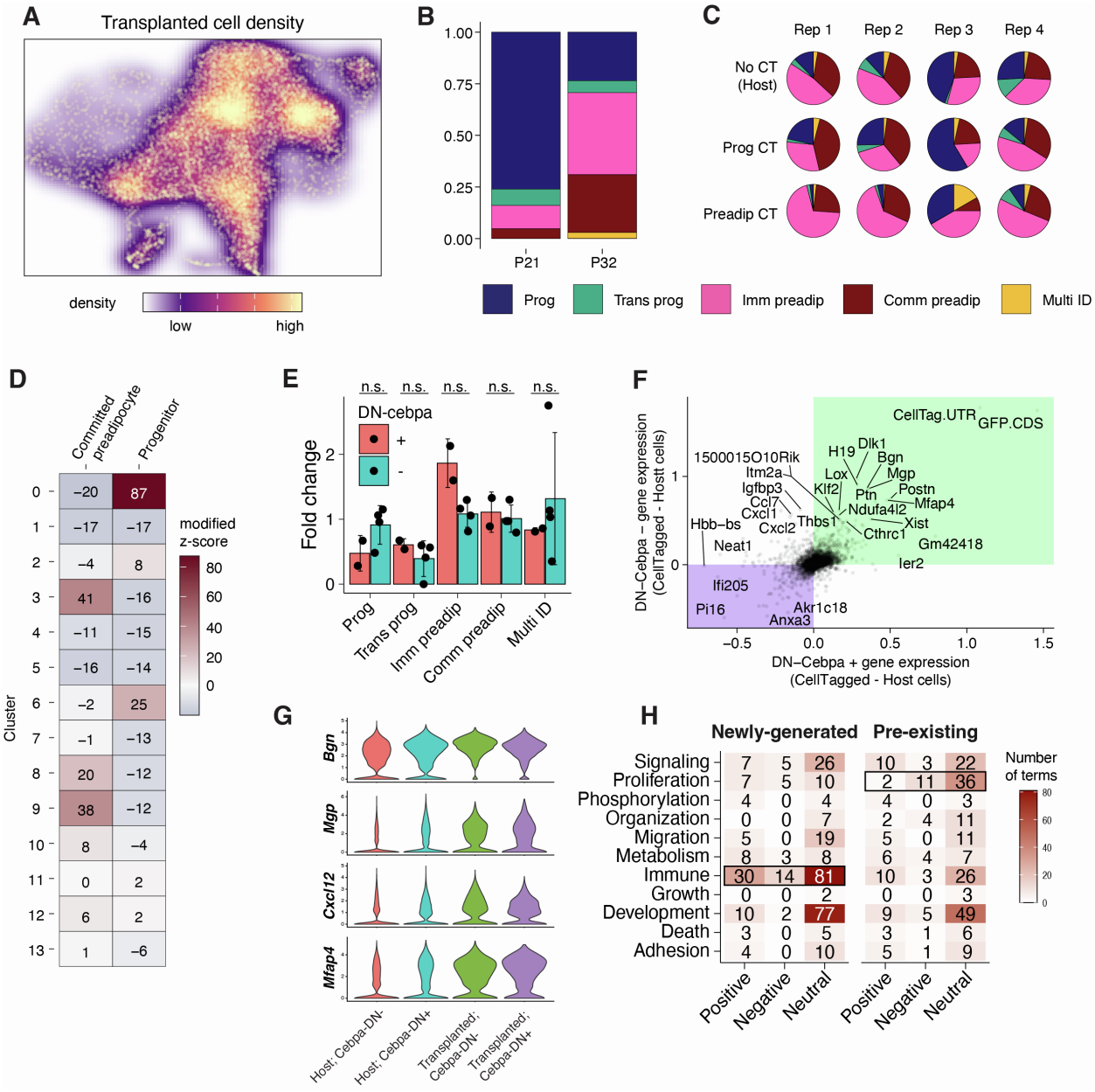

Figure S4. CellTag data enables illustration of the divergent potential of distinct preadipocyte populations.

(**A**) Heatmap depicting the distribution of transplanted GFP and/or CellTag-expressing cells within the integrated UMAP space.

(**B**) Comparison of cell type proportions in skin APCs (classified manually or via Capybara using the P21 APC skin reference) before and after the initiation of the hair follicle anagen phase.

(**C**) Capybara-classified cell type proportions for each biological replicate, distinguishing transplanted (CellTagged) and host (non-CellTagged) populations, using P21 skin APCs as reference.

(**D**) Modified z-scores representing the Jaccard similarity of each cluster in the P32 APC dataset

compared to progenitor or committed preadipocyte identities. Background distributions were derived from 1,000 randomized permutations.
(**E**) Fold change in cell type proportions comparing DN-CEBPA+ and DN-CEBPA– transplanted cells relative to their host populations. Data represent 6 biological replicates; analyzed via unpaired two-sample *t*-test with Welch's correction.
(**F**) Scatter plot illustrating differential normalized gene expression between CellTagged and host cells under DN-CEBPA+ and DN-CEBPA– conditions. Features in the green quadrant are upregulated in CellTagged cells; features in the purple quadrant are elevated in host cells. Highlighted genes show an absolute expression difference exceeding 0.5 normalized counts per cell under either DN-CEBPA condition.
(**G**) Violin plots showing expression of key adipocyte marker genes in DN-CEBPA+ and DN-CEBPA– conditions.
(**H**) Gene ontology (GO) analysis of differentially expressed genes between newly generated and pre-existing immature preadipocytes. Terms are categorized by their positive, negative, or neutral impact on the indicated biological processes.

Figure S5 (Related to Figure 5)

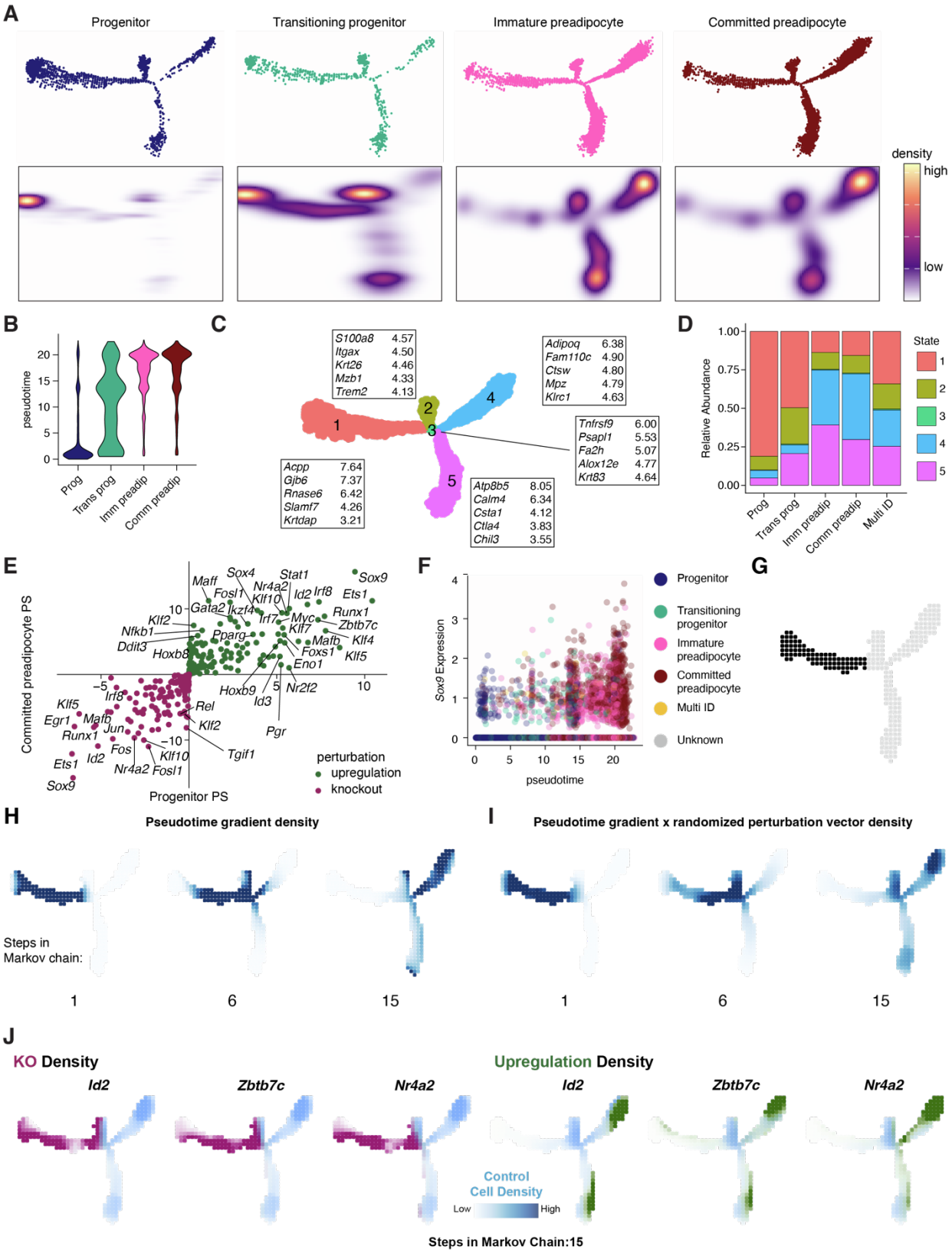

Figure S5. CellOracle prioritization of TFs driving the progenitor to preadipocyte transition.
(**A**) Monocle embedding of P32 APCs (top) and corresponding density projections of individual APC cell types (bottom): progenitors, transitioning progenitors, immature preadipocytes, and committed preadipocytes.
(**B**) Distribution of pseudotime values for each APC cell type calculated by DDRTree.
(**C**) Monocle embedding of P32 APCs colored by Monocle-defined states, with the top 5 significantly enriched genes per state, ranked by positive fold change (expression in state relative to aggregate of remaining states).
(**D**) Relative abundance of Monocle states across APC cell types. Each embedding branch (state) is modestly enriched in a particular cell type (e.g., progenitors localized to state 1). Branching structure was independent of CellTagging (data not shown) and does not represent terminal differentiation states.
(**E**) CellOracle TF perturbation scores for progenitors and committed preadipocytes, comparing systematic TF upregulation (green) and knockout (magenta) perturbations.
(**F**) Normalized *Sox9* expression versus pseudotime in P32 APCs, colored by APC cell type.
(**G**) Region of Monocle2 embedding (state 1) selected for Markov simulation analyses.
(**H**) Density plots showing Markov simulations of the pseudotime gradient vector field after 1, 6, and 15 Markov steps within the selected embedding region in (G).
(**I**) Density plots showing Markov simulations combining pseudotime gradient and randomized vector fields after 1, 6, and 15 Markov steps within the selected region in (G).
(**J**) Density plots for Markov simulations of TFs *Id2, Zbtb7c*, and *Nr4a2*, overlaid on pseudotime gradient/randomized vector field simulation (blue) after 15 Markov steps within the embedding region in (G).

Figure S6 (Related to Figure 6)

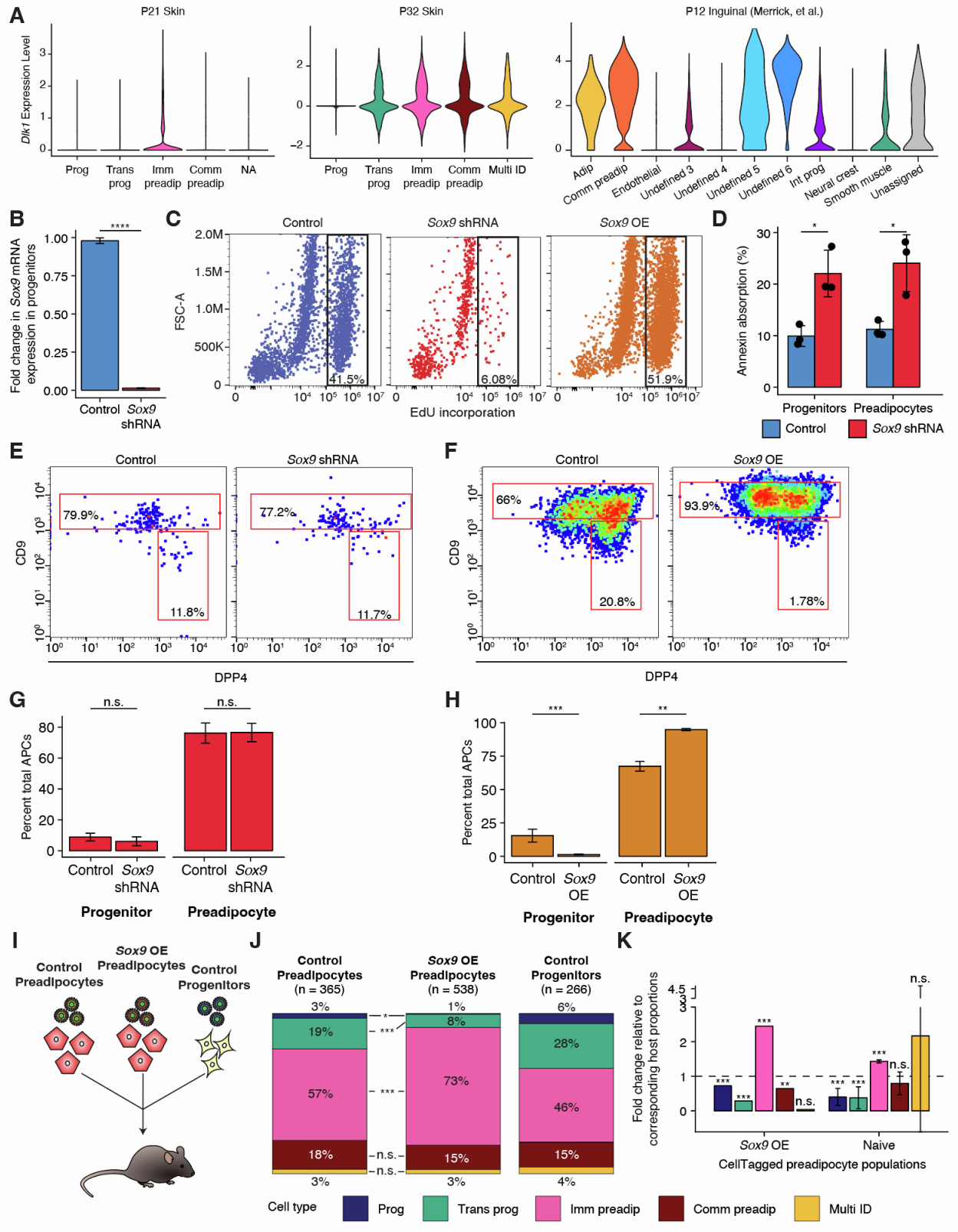

Figure S6. *Sox9* overexpression confers a proliferative advantage upon skin progenitors alone.

(**A**) Normalized *Dlk1* expression by cell type in skin APCs at P21 (left), skin APCs at P32 (center), and inguinal APCs at P12 (Merrick et al., right).

(**B**) Relative *Sox9* expression (qPCR) in progenitors transduced with control (scrambled shRNA + GFP) or Sox9 shRNA after 5–7 days ($p = 9.75 \times 10^{-5}$, two-tailed unpaired *t*-test with Welch's correction; n = 3 technical replicates; ****p < 0.0001).

(**C**) Representative FACS plots of EdU incorporation in isolated progenitors transduced with control, *Sox9* overexpression (OE), or *Sox9* knockdown (KD) lentiviruses (day 5 post-transduction).

(**D**) Annexin V staining quantification indicating apoptosis in progenitors and preadipocytes after control or *Sox9*-KD treatments (p = 0.0282 (progenitors), p = 0.0478 (preadipocytes), two-tailed unpaired *t*-test with Welch's correction; n = 3 biological replicates; *p < 0.05).

(**E**) Flow cytometry of DPP4 and CD9 in CellTagged APCs transduced with an empty CellTag library (left) or library including *Sox9*-shRNA (right).

(**F**) Flow cytometry assessing differentiation (DPP4/CD9 expression) of transplanted Lin-/CD34+/CD29+/GFP+ progenitor cells expressing control or *Sox9*-OE lentiviruses, harvested 11 days post-transplantation.

(**G, H**) Quantification of preadipocyte and progenitor identities by FACS after transplantation of *Sox9*-KD (G) or *Sox9*-OE (H) progenitors. *Sox9*-KD showed nonsignificant differences in CD9 expression; *Sox9*-OE induced a significant decrease in $CD9^{low}$ progenitor cells and increased $CD9^{high}$ preadipocytes (G: p = 0.1547 progenitor, p = 0.9261 preadipocyte; H: ***$p = 6.08 \times 10^{-4}$ progenitor, *$p = 1.25 \times 10^{-3}$ preadipocyte, two-tailed unpaired *t*-test with Welch's correction).

(**I**) Experimental scheme for testing *Sox9*-OE in preadipocytes. Isolated preadipocytes were treated with *Sox9*-shRNA, control-shRNA+GFP, or *Sox9*-OE, mixed equally, transplanted into P21 mouse skin, and recovered at P32 (n = 1 biological replicate).

(**J**) Cell type proportions identified by Capybara in CellTagged populations (P21 reference dataset). *Sox9*-OE preadipocytes showed a significant increase in immature preadipocytes relative to control preadipocytes (randomization test, Bonferroni-corrected; progenitor *$p = 4.4 \times 10^{-3}$, transitioning progenitor and immature preadipocyte **$p < 0.0001$, committed preadipocyte p = 0.2693, multi ID p = 1.000). Total cells recovered: *Sox9*-OE preadipocytes (n=538), control preadipocytes (n=365), and control progenitors (n=266).

(**K**) Proportions of Capybara-classified cell types originating from preadipocytes comparing *Sox9*-OE preadipocytes versus previously isolated CD9+ control preadipocytes at P32. *Sox9*-OE preadipocytes exhibited an increased proportion of immature preadipocytes and reduced committed preadipocytes, indicating *Sox9*-OE does not impair preadipocyte differentiation potential but biases cells toward a less mature state (randomization test, Bonferroni-corrected; ***p < 0.0001 progenitor, transitioning progenitor, immature preadipocyte; **p = 0.0001 committed preadipocyte; multi ID p = 0.273; see Figure 4F for comparison p-values).

Figure S7 (Related to Figure 7)

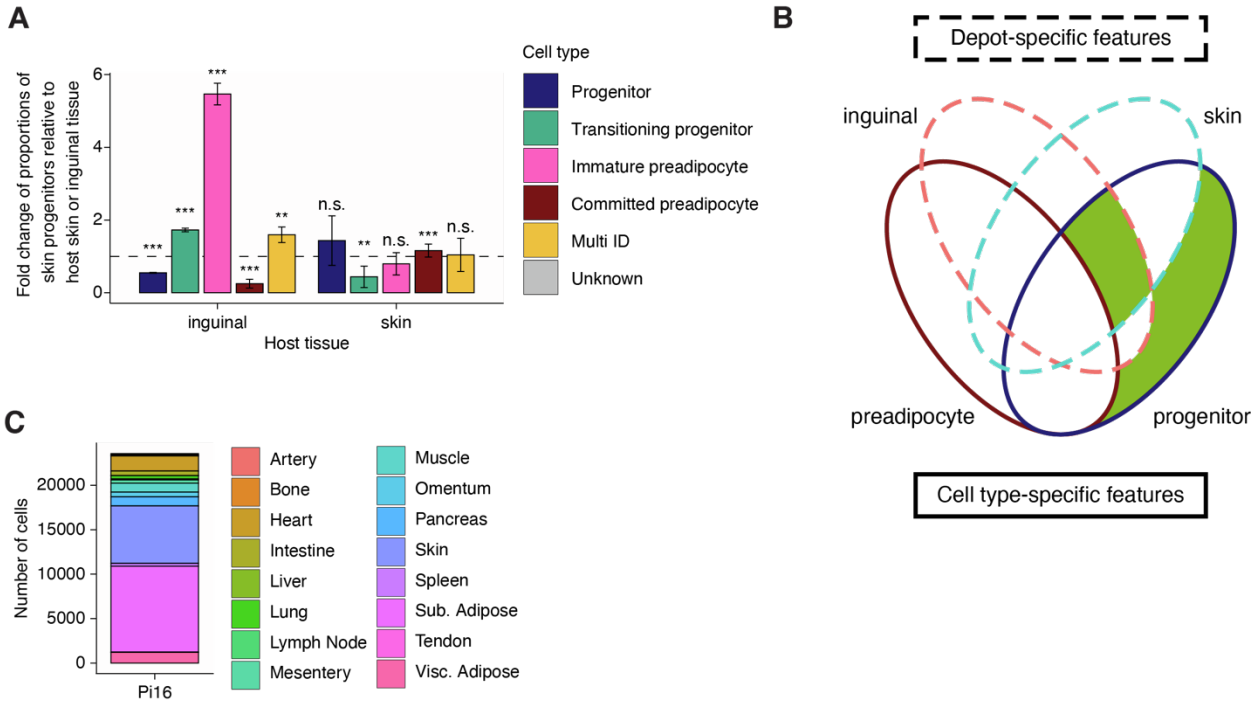

Figure S7. Skin progenitors transplanted into inguinal adipose tissue produce a significantly enriched population of immature preadipocytes.

(**A**) Fold-change comparison of cell-type proportions (classified by Capybara) of transplanted skin progenitors recovered from inguinal adipose versus skin tissue (11 days, P21→P32). Skin progenitors transplanted into inguinal adipose showed significant enrichment of immature preadipocytes compared to skin transplants (randomization test, Bonferroni-corrected; progenitor, transitioning progenitor, immature preadipocyte, committed preadipocyte: ***p < 0.0001; multi-ID: **p = 0.0005; see Figure 4F for skin-transplant control p-values).

(**B**) Workflow schematic illustrating differential expression analyses used to identify intrinsic gene expression signatures in skin progenitor populations.

(**C**) Tissue-origin composition of the Pi16+ adipocyte precursor cluster as identified in the dataset from Buechler et al.